Alma Mater Studiorum – Università di Bologna

Dipartimento di Fisica e Astronomia
Corso di Laurea magistrale in Astrofisica e Cosmologia

Probing the accretion/ejection flows in AGN by characterizing Fe K emission/absorption line variability with residual maps

Tesi di laurea

Presentata da:
Deborah Costanzo

Relatore:
Chiar.mo Prof. Cristian Vignali

Correlatore:
Dott. Massimo Cappi
Dott. Mauro Dadina
Dott. Barbara De Marco

Appello II
Anno accademico 2017-2018

Sommario

La dinamica e la geometria del materiale nelle vicinanze di un buco nero supermassiccio (SMBH) nei nuclei galattici attivi (AGN) sono ancora incerte, sia per quanto riguarda gli inflow sia per gli outflow legati al disco di accrescimento. Questi ultimi fenomeni possono avere un ruolo fondamentale per quanto riguarda il feedback da AGN sulla galassia ospite. Per questo motivo risulta essenziale capirne le proprietà e l'estensione spaziale. L'osservazione simultanea di strutture in emissione ed assorbimento fornisce inoltre elementi utili per capire quanto i processi sottostanti siano connessi tra di loro e, di conseguenza, i meccanismi che li originano. L'analisi spettrale temporalmente risolta è fondamentale per studiare questi fenomeni.

La banda energetica 4-10 keV è quella piú adatta per il raggiungimento degli obiettivi sopra citati, in quanto include la riga di fluorescenza del ferro a 6.4 keV (che fornisce informazioni sui moti intorno al SMBH) e possibilmente righe risonanti in assorbimento del ferro blueshiftate, indicative della presenza di venti da disco ultra-veloci (v dell'ordine di 0.1 c, i cosiddetti UFOs, osservati in circa il 50% della popolazione di AGN locali per cui esistono dati in banda X di buona qualità).

L'analisi adottata in questo lavoro di tesi si basa sulla tecnica dell'Excess Map, introdotta da Iwasawa et al. (2004). Lunghe esposizioni sono sezionate in intervalli temporali e ogni spettro risultante è fittato con un semplice modello di continuo. I residui positivi sono quindi utilizzati per costruire un'immagine nel piano tempo vs. energia al fine di massimizzare la rivelazione di possibili strutture spettrali e derivarne l'evoluzione temporale. Questo è possibile in quanto l'informazione temporale è accoppiata all'analisi spettrale. Laddove nelle Excess Map solo i residui positivi venivano considerati, tramite la nostra tecnica, denominata Residual Map, anche i residui negativi, legati a possibili strutture in assorbimento, vengono individuati e analizzati.

Si è selezionato un campione di galassie di Seyfert di tipo 1 osservate con il satellite XMM-Newton, che garantisce la massima sensibilità nell'intervallo spettrale di interesse per il nostro studio. Questa sua proprietà permette di ottenere un elevato numero di conteggi anche integrando su intervalli temporali corti. In particolare, dal catalogo 3XMM-DR7 si sono scelte le sorgenti piú brillanti nelle bande di interesse, NGC3783 e Mrk 509; flusso

in band 4.5–12 keV di circa 10^{-11} erg cm^{-2} s^{-1}) e IRAS 13224-3809, ossia quella con l'osservazione piú lunga al momento disponibile, essendo stata osservata per 2Ms (flusso in banda 4.5–12 keV di circa 10^{-13} erg cm^{-2} s^{-1}).

Un limite di questa tecnica risulta essere che, con i telescopi in banda X attualmente disponibili, essa può essere applicata solo su un numero limitato di sorgenti, in quanto è necessario avere un numero minimo di fotoni in ogni bin temporale/spettrale. Pertanto, se si vogliono studiare tempi scala corti e righe spettrali strette, si possono analizzare solo sorgenti brillanti.

Per le due sorgenti a piú elevato flusso riusciamo a studiare scale temporali dell'ordine di 2.5 ks e risoluzioni energetiche di 100 eV. Per IRAS 13224-3809, invece, questo non è stato possibile, limitando pertanto lo studio a tempi scala molto piú lunghi e perdendo la sensibilità verso le righe piú strette.

Abbiamo verificato la bontà di questa tecnica attraverso test statistici e tramite confronti con analisi spettrale classica in banda X.

A causa del limitato tempo a disposizione, ci si è focalizzati su un'osservazione particolarmente interessante tra quelle relative a NGC3783; in questa la riga del Ferro Kα mostra quattro picchi intervallati da circa 5–10 ks, corrispondenti a tempi orbitali di un hot spot co-ruotante con il disco di accrescimento a distanze di circa 9-30 raggi gravitazionali.

Uno dei prossimi passi in questo tipo di studio richiede sicuramente l'adozione di appropriati modelli spettrali per riprodurre i dati al meglio e capire quali fenomeni siano in atto. In tal senso, l'analisi condotta in questa tesi rappresenta un punto essenziale per capire se sussiste variabilità nelle righe in emissione e in assorbimento e i relativi tempi scala, capace di fornire spunti sulle componenti necessarie per ottenere una buona riproduzione spettrale dei dati stessi.

Nei prossimi anni XMM-Newton continuerà ad acquisire dati di buona qualità, rendendo possibile il monitoraggio di sorgenti brillanti a cui applicare questo tipo di analisi in attesa dei telescopi in banda X di prossima generazione. A tal proposito nel 2021 XRISM, in virtù di un'eccellente risoluzione spettrale, sarà capace di risolvere righe molto strette (fino a quelche eV) per le sorgenti piú brillanti; nel 2028 Athena, grazie anche ad'elevata sensibilità (0.25 m^2 a 6 keV), permetterà di utilizzare la tecnica della Residual Maps su un numero molto maggiore di sorgenti, anche a flussi minori rispetto a quelli attualmente permessi da XMM-Newton, e anche su scale temporali piú corte. Nel frattempo si cercherà di migliorare questa tecnica a cominciare da un'analisi sistematica dei set di dati presentati in questo lavoro di tesi, per capirne l'efficacia dell'approccio adottato e, possibilmente, ricavare informazioni importanti sui processi di accrescimento e di outflows nelle regioni piú interne degli AGN.

Abstract

The dynamics and geometry of the material close to the Super Massive Black Hole (SMBH) in Active Galactic Nuclei (AGN) are still largely uncertain, both as regards the inflows via accretion disk and the outflows. The latter phenomena may have a fundamental role in the AGN feedback on the host galaxy, so it is important to understand their properties and their extent. A simultaneous investigation of these flows can bring to some kind of correlation, that shall help unravel the driving mechanisms of massive winds from the disk. This is still an open issue in the field of high-energy astrophysics. Time-resolved spectral analysis is a key tool to investigate these phenomena. The 4.0-10.0 keV energy band is the most suitable for these aims, because it includes the Fe Kα fluorescence emission line at 6.4 keV, a fundamental proxy of the motions around the SMBH, and possibly Fe resonant absorption lines, features that indicate the presence of massive, relativistic ($<$v$>\sim$0.1 c) disk winds (Ultra Fast Outflows, UFOs), observed in about 50% of local AGN for which good quality data exist.

The analysis we adopt is bases on the *Excess Map* technique introduced by Iwasawa et al. (2004). Long exposures are sliced in time bins and each spectrum is fitted with simple models accounting only for the continuum emission; the positive residuals are then used to build up an image in the time vs. energy domain to maximize the detection of possible spectral features and derive their evolution. This is made possible by coupling time and spectral analysis. While in Excess maps only the positive residuals are used, in our upgraded *Residual Map* technique we map the negative residuals as well, mapping simultaneously the absorption and emission features.

We selected a sample of Seyfert 1 galaxies observed with XMM-*Newton*, i.e. the telescope with the highest sensitivity in our spectral range of interest, in order to have the largest possible number of photons in the shortest possible time bins. In particular, from the 3XMM-DR7 catalogue we chose the brightest sources in our energy bands (i.e. NGC 3783 and Mrk 509, $F_{4.5-12\,\mathrm{keV}} \sim 10^{-11}$ erg s^{-1}cm^{-2}) and the source with the longest total exposure (i.e. IRAS 13224-3809, over 2Ms of exposure, $F_{4.5-12\,\mathrm{keV}} \sim 10^{-13}$ erg s^{-1}cm^{-2}). A limitation of this technique is that, with the current available

X-ray telescopes, it can be applied only to a small number of sources. In fact, we have to grant a minimum of photons per time/energy bin and if we want to probe short time scales and/or narrow spectral features, we can only use sources with a high flux. We found that for the two bright sources it is possible to probe time scales as short as 2.5 ks and energy resolutions of 100 eV. However, for IRAS 13224-3809, it was not possible to achieve such fine resolutions and we are limited to carry our variability analysis on longer time scales, thus losing information on the narrowest features because of the low flux of this source.

We verified the reliability of our technique both with statistical tests and with a direct comparison with classical X-ray spectral analysis.

We could not carry out a complete analysis of all our datasets because of time issues, so we focused only on one of the observations of NCG 3783, which showed interesting peculiarities. In it we identified four Fe Kα line high peaks spaced out by fairly regular time intervals of $\sim$ 5-10 ks, corresponding to the orbital period of an emitting region at a distance in the range of $\sim$9-30 r_g from the SMBH, if interpreted as a hot spot co-rotating with the accretion disk.
For Mkr 509 we only performed a quick spectral analysis, focusing on one dataset, whose residual map showed complex residual features in the whole map and a prominent Fe Kα component only in the second part of the observation. We only verified the presence of this change also in the spectra.
A more complex spectral modeling is certainly needed to further characterize the sources and the physical phenomena in act. However, our residual maps are important since they can give an immediate idea of the variability of the emission/absorption features and their time scales, and also provide hints of the components to use in the detailed spectral analysis.

XMM-*Newton* is continuing to acquire high-quality data, so it will be possible to monitor the bright sources with this kind of analysis while waiting for next-generation X-ray telescopes. In this regard, in 2021 *XRISM* (X-Ray Imaging and Spectroscopy Mission), thanks to the excellent spectral resolution of its detectors, will allow us to resolve features as narrow as few eV for the brightest sources in the 0.3-12 keV energy band, and in 2028 *ATHENA* (Advanced Telescope for High Energy Astrophysics) with its unparalleled sensitivity (A_{eff} $\sim$0.25 m^2 at 6 keV), will allow us to use the Residual Map analysis on a much larger number of sources with a lower flux and/or probe shorter time scales.

In the meanwhile, we will try to improve the Residual Maps technique and, starting from the datasets in our sample that we have not properly analyzed yet, to further verify the effectiveness of the method and possibly derive important information on the accretion/ejection flows in the innermost regions of the AGN.

Contents

1 Active Galactic Nuclei **9**
- 1.1 The AGN Paradigm . . . 9
- 1.2 AGN Structure . . . 10
- 1.3 Seyfert 1 X-ray spectrum . . . 14
  - 1.3.1 Emission lines . . . 17
  - 1.3.2 Absorption . . . 20
- 1.4 Variability . . . 24

2 Residual maps **27**
- 2.1 Method . . . 28
  - 2.1.1 Time resolution . . . 28
  - 2.1.2 Energy resolution . . . 29
- 2.2 How to read a residual map . . . 29

3 XMM-*Newton* and source sample selection **35**
- 3.1 The telescopes . . . 35
- 3.2 The on-board instruments . . . 37
- 3.3 The 3XMM-DR7 catalogue . . . 38
- 3.4 Source sample selection criteria . . . 39
  - 3.4.1 Selected sources . . . 40

4 NGC 3783 **43**
- 4.1 Observations and data reduction . . . 44
- 4.2 Residual Maps . . . 45
  - 4.2.1 Observation 3120 . . . 47

5 Mrk 509 **57**
- 5.1 Observations and data reduction . . . 57
- 5.2 Residual Maps . . . 58
  - 5.2.1 Observation 1813 . . . 65

6 IRAS 13224-3809 **69**
- 6.1 Observations and data reduction . . . 69
- 6.2 Excess maps applicability . . . 70

7 Reliability of the residual map method **77**
7.0.1 Excess/absorption "balance" 77
7.0.2 Residual light curves 80
7.0.3 Photon index vs N_H 81
7.0.4 Photon index vs line intensity 81

8 Conclusions and future prospectives **89**

Bibliography **98**

Chapter 1

Active Galactic Nuclei

About 10% of all galaxies show a large luminosity (up to $L_{bol} \approx 10^{48}$ erg s^{-1}, with typical values of $L_{bol} \approx 10^{44} - 10^{46}$ erg s^{-1}) (e.g. Padovani et al. (2017)) over the whole electromagnetic spectrum, originated from highly energetic phenomena in the central regions. These sources are called Active Galactic Nuclei (AGN). The radiation produced in the nuclear regions of the AGN can exceed that of the entire host galaxy, overcoming all the light from the galaxy stellar component.

1.1 The AGN Paradigm

The most recognized model to explain the large quantity of radiation observed in AGN postulates that the emission is due to material accreting onto a super massive black hole (SMBH) at the center of the galaxy, with a mass typically in the range $10^6 - 10^9$ $M_\odot$ (e.g. Peterson (1997)).

Accretion onto compact objects is the most efficient mechanism to convert mass into radiation. The conversion has an efficiency η, so the total available energy is $E = \eta Mc^2$. The rate by which this energy is radiated is $L = dE/dt = \eta \dot{M} c^2$, where $\dot{M} = dM/dt$ is the mass accretion rate. The potential energy of a mass m falling from a distance r onto an object of mass M can be converted to radiation at a rate of:

$$L = \frac{dU}{dt} = \frac{GM}{r}\frac{dm}{dt} = \frac{GM\dot{M}}{r} \tag{1.1}$$

Therefore $\eta \propto M/r$, which is a measure of the compactness of the source: the smaller the system the higher the efficiency. For SMBHs in AGN $\eta \approx 0.1$.

A simple estimate of the mass of the central object can be made assuming a completely ionized gas falling with spherical symmetry at a constant rate. To maintain the stability of the system, the outward radiation pressure force

must be compensated by the inward gravitational attraction.[1] The module of the radiation force on a single electron, given the Thomson cross-section σ_e for the interaction with a photon, is:

$$F_{rad} = \sigma_e \frac{L}{4\pi r^2 c} \tag{1.2}$$

while for the gravitational force we have:

$$F_{grav} = \frac{GMm_p}{r^2} \tag{1.3}$$

The Eddington limit is the maximum luminosity for an accreting object above which the system would interrupt the accretion; for a central object of mass M expressed in solar masses we have:

$$L_{Edd} = \frac{4\pi G c m_p}{\sigma_e} M \approx 1.26 \times 10^{38} \left(\frac{M}{M_\odot}\right) ergs^{-1} \tag{1.4}$$

The Eddington limit allows us to calculate the minimum mass to have accretion with a luminosity of the order of $10^{44}\ erg\ s^{-1}$:

$$M_{Edd} = 8 \times 10^5\ L_{44}\ M_\odot \tag{1.5}$$

Should a typical quasar have a luminosity of $10^{46}\ erg\ s^{-1}$, the central object should have a mass of $\approx 10^8 M_\odot$. AGN present variability on different time scales and some show significant flux variations on time scales of days, hours and even minutes. The variability time scale constrains the size of the regions that produce such variations, which can be as small as the Solar System. Such a mass contained in such a limited region indicates that the central object has to be a SMBH.

1.2 AGN Structure

The physical structure of AGN is still not completely determined, but the majority of models predicts a structure consisting, at least, of the following components.

- **Accretion Disk**
  The spherical symmetry for the infall is a simplistic hypothesis and does not represent well the reality: the material preserves its angular momentum, so it will form an *accretion disk* around the black hole. Viscous forces transfer the angular momentum outward and the flow spirals inward, dissipating part of its gravitational potential energy

[1] The radiation force on a proton and the gravitational force on an electron are negligible, due to their different masses: $m_p/m_e \approx 10^3$.

into kinetic energy. A complete description of the disk structure is hard to model, since it depends on many parameters (e.g. magnetic fields, viscosity, accretion rate, etc.), but it is possible to describe it as geometrically thin and optically thick disk, so the emission can be approximated as blackbody. From the virial theorem, the gravitation potential energy is released at the rate $dU/dt = GM\dot{M}/r$: half of it heats up the disk and half is radiated as luminosity L. Using the Stefan-Boltzmann law, the energy radiated is σT^4 for the two sides of the disk, each with an area of πr^2. Therefore we have:

$$L = \frac{GM\dot{M}}{2r} = 2\pi r^2 \sigma T^4 \tag{1.6}$$

Solving for the temperature at the distance r from the center:

$$T = \left(\frac{GM\dot{M}}{4\pi\sigma r^3}\right)^{1/4} \tag{1.7}$$

The temperature is in the range of $10^5 - 10^6$ K, grows towards the center of the disk and so does the emission frequency: for a blackbody we obtain $\nu_{\max} \propto \mathrm{kT/h} \propto \mathrm{r}^{-3/4}$. The most internal regions around a SMBH of about $10^8 M_\odot$ can reach frequencies in the extreme UV band ($\nu_{max} \sim 10^{16}\ Hz$). Integrating over all radii, we see a sum of blackbody spectra at different temperatures, called *Big Blue Bump*, in the optical/UV continuum (at wavelengths of few thousands Å).

- **Hot Corona**
  The disk is surrounded by a *corona* of hot, ionized, optically thin gas. The precise location of the corona is still unknown; it is reasonable to assume the corona very close to the accretion disk, probably above it. Its high temperature ($T \sim 10^9\ K$) is most likely due to magnetic reconnection phenomena.

- **Broad Line Region (BLR)**
  It is composed by a number of gas clouds located in proximity of the central source. The gas reprocesses the optical/UV radiation through permitted emission lines from recombination and de-excitation. Forbidden lines are not produced because of the high electron density (10^9 cm^{-3}). The temperature of the BLR is $\sim 10^4$ K. The lines are broadened by Doppler effect; widths span from $\Delta \mathrm{v_{FWHM}} \sim 500$ km s^{-1} to $\Delta \mathrm{v_{FWHM}} \gtrsim 10^4$ km s^{-1}, with typical values of $\Delta \mathrm{v_{FWHM}} \sim 5000$ km s^{-1}. Motions in this region can be used as a probe of the dynamics in the SMBH gravitational well and to estimate the mass of the black hole.

- **Narrow Line Region**
  It consists of gas clouds at temperatures of 10000 – 25000 K. Densities

are lower (10^4 cm^{-3}) than those of the BLR, thus allowing for the production of forbidden emission lines. The bulk velocities are also lower than in the BLR: $200 \gtrsim \Delta v_{FWHM} \gtrsim 900$ km s^{-1}, with average values of $\Delta v_{FWHM} \sim 400$ km s^{-1}. This region is spatially resolved in the optical band: it often manifests itself with an axis-symmetric morphology with two ionization cones centered in the nuclear source.

- **Torus**
  It is composed mainly by molecular gas and dust. There are still many uncertainties about the geometry of the torus, in particular whether the material has a smooth or clumpy distribution, and whether there is actually a physical separation from the disk (the alternative hypothesis is that the torus is just the continuation of the disk). Furthermore, the physical extension of the torus is still matter of debate. The torus absorbs optical and UV radiation and reprocesses it via thermal emission in the mid-infrared band, peaking at wavelengths of few tens of micron.

- **Jets**
  Relativistic jets are present in about 10% of AGN. The mechanism responsible for the jets is still uncertain, but is probably related to the magnetic fields of the black hole and/or of the disk. Jets originate in the central region and are expected to be aligned with the symmetry axis of the system. They are formed of charged particles and emit mostly via synchrotron mechanism, from the radio to the γ-ray band. In face-on AGN (where the observer has potentially a direct view of the nucleus), relativity effects boost the brightness of the approaching jet with respect to the receding one.

Component	Size
SMBH	$R_S \sim 0.01$ - 10 AU
Accretion disk	$R_{in} \sim 0.01$ - 60 AU
	$R_{out} \sim 1$ - 1000 AU
Broad line region	$R_{BLR} \sim 0.01$ - 1 pc
Torus	$R_{torus} \sim 1$ - 10 pc
Narrow line region	$R_{NLR} \sim 10^2$ - 10^4 pc
Jet	$R_{jet} \sim 10^2$ - 10^3 kpc

Table 1.1: Extents of AGN components. $R_s = 2GM_{BH}/c^2$ represents the Schwarzschild Radius.

In Figure 1.1 we can see a representation of the overall AGN structure and its components, whose indicative sizes are reported in Tab. 1.1.

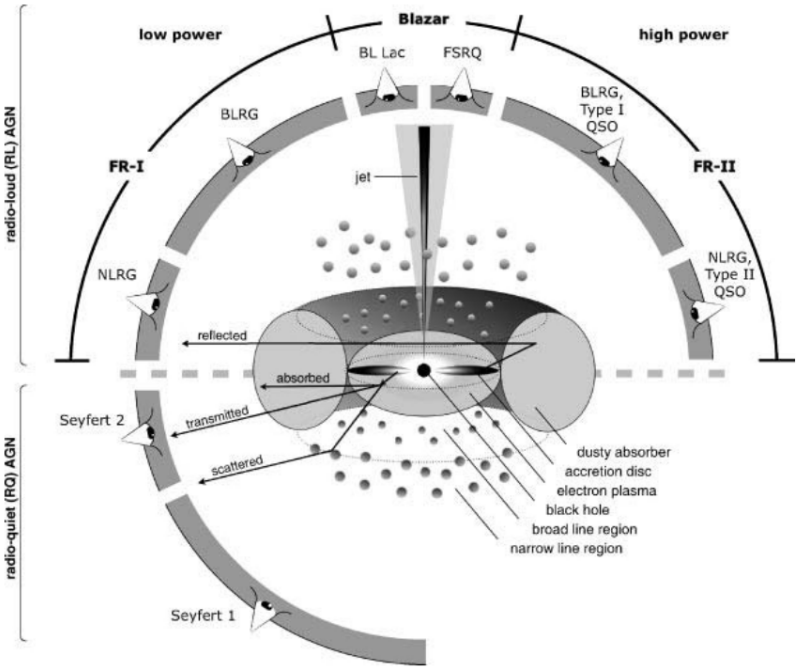

Figure 1.1: Representation of the AGN structure and its components. It is shown how the line of sight can affect the view of the internal regions and so the classification of the object. Image from Beckmann and Shrader (2013).

The AGN is typically represented as an axis-symmetric system, so observing it from different directions (i.e., along different lines of sight) allows to see different parts, each with its characteristic emission. Even though the classes of objects identified as AGN may appear very heterogeneous, most of their differences can be explained as due to changes in just a few of these parameters: orientation (see Fig. 1.1), accretion rate, presence - or absence - of jets and, possibly, the environment and the host galaxy (Padovani et al., 2017). The so-called Unification Model of AGN is based on the fact that the AGN engine (i.e., accretion onto a SMBH) is the same for most AGN, but orientation effects play a major role in their classification.

1.3 Seyfert 1 X-ray spectrum

The X-ray spectrum of radio-quiet type 1 AGN (i.e. Seyfert 1 galaxies), in the energy band 0.1-100 keV, can be modeled at a first order as a power law, such as:

$$F(E) \propto E^{-\Gamma} \tag{1.8}$$

where F(E) is the flux in units of photons cm^{-2} s^{-1} keV^{-1}. The photon index Γ assumes typical values of $\sim 1.7 - 1.9$.

However, a deeper investigation indicates the presence of additional components, in excess or absorption with respect to the primary power law. They are easily detectable in type 1 objects because the X-ray emission from the innermost region is only mildly absorbed. These components arise from specific structures, whose properties can be derived using X-ray spectral analysis. The typical X-ray spectrum of these sources is shown in Fig. 1.2.

The typical features that we can observe in unobscured type 1 AGN are:

- The **Soft excess** is a strong emission in excess of the power law continuum, at energies of$\sim$ $0.1 - 2.0$ keV. Its origin is still unclear: some models attribute it to the thermal emission of the inner and hotter part of the accretion disk, other invoke the presence of either a warm corona or an ionized, possibly relativistic reflection component. Its peculiarity is that for different sources, if fitted with a thermal model, it shows a notably constant temperature, despite differences in the central object masses and in luminosities, suggesting that it is most likely not directly ascribed to accretion disk emission.

- **Photoelectric absorption** due to neutral material. It can be ascribed to gas contained in our galaxy, with typical column densities of $\mathrm{N}_H \approx 10^{20}$ cm^{-2}, as well as to gas contained in the source, with column densities up to $\mathrm{N}_H \sim 10^{22}$ cm^{-2} (in type 1 Seyferts) and up to $\mathrm{N}_H \sim 10^{24}$ cm^{-2} (in type 2 Seyferts), likely related to the torus.

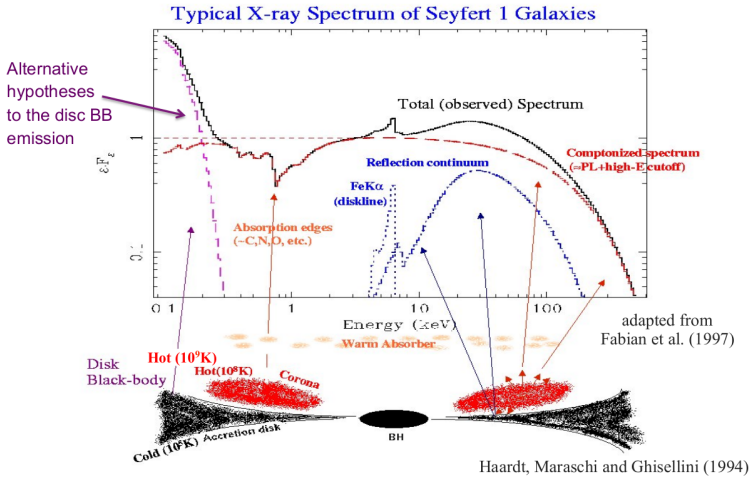

Figure 1.2: The X-ray spectrum of a Seyfert 1 galaxy, in which all the typical features are highlighted with different colors and linked to the component that produces them, in the simplified structure pictured below.

- The **Warm absorber** is composed of partially ionized, optically thin material along the line of sight. It causes the relatively strong absorption features observed in about half of the Seyfert galaxies in the energy range 0.1–2.0 keV. Its column density can reach $N_H \gtrsim 10^{23}$ cm^{-2}. The precise location and geometry of this gas are not completely clear, although it is supposed to be formed of distinct components, with different densities and properties as a function of the distance from the black hole (Reynolds, 1997).

- The **Compton reflection component**, characterized by a flattening of the spectrum for energies above 10 keV, with a peak between 30 and 50 keV (the *Refection Hump*) and fluorescence lines between 0.1-8 keV from the most abundant elements, such as Fe, C, O, Mg, Cr, Ni. The most prominent features are due to Fe: the Fe Kα line at ∼6.4 keV, the absorption edge at ∼7.1 keV and, possibly, the Kβ line at ∼7.05 keV. The lines are due to fluorescence and are thought to be directly connected with the reflection hump. The physical origin is Compton reflection from an optically thick gas that should be relatively cold, probably associated with the accretion disk or the molecular torus, illuminated by the primary source of X radiation (i.e. the power law).

- A **Cut-off** on power law at energies around $\sim 100 - 200$ keV, that causes a sudden decrease in the flux. This is ascribed to the thermal Comptonization which is responsible for the primary power law emission.

Once these components are considered in the X-ray spectral modeling,

the photon index (Γ) of the power law settles to an average value of ~ 1.9 (Mushotzky et al., 1993).

Two-phase model The most accepted model to explain the production of the power law component observed in AGN is the *two-phase model* (Haardt and Maraschi (1991); Haardt and Maraschi (1993)), which provides explanations for the AGN components already described in Sect. 1.2. This model predicts an emission region formed by two distinct structures: the accretion disk, geometrically thin and optically thick ($\tau > 1$) and relatively cold ($T_d \sim 10^5 - 10^6$ K), and above it the corona, being optically thin ($\tau < 1$), hot ($T_c \sim 10^9$ K, $kT_c \sim 100$ keV) and ionized. From the equipartition of the kinetic energy among the electrons $\frac{m_e v_e^2}{2} = \frac{3kT}{2}$, we have $\beta = \frac{v}{c} = \sqrt{\frac{3kT}{m_e c^2}} \sim 0.7$, corresponding to a Lorentz factor $\gamma = 1/\sqrt{1-\beta^2} \sim 1.4$.

The interaction of these two "phases" leads to a rather complex emission mechanism that we summarize in the following three points:

- The inner regions of the accretion disk produce a black body emission peaking in the optical/UV for reasonably high black hole masses, as observed in AGN.

- Part of this low-energy radiation ($E_{phot} \ll kT_c$) interacts via Inverse Compton with the electron population in the corona and is upscattered towards higher energies. In fact, in every collision there is an energy exchange from the electron to the photon of about $\Delta E_{phot} \simeq \gamma^2 E_{phot} \sim 2E_{phot}$. This represents the most efficient cooling process in the corona. The resulting spectral profile follows a power law with $\Gamma \sim 1.9$, up to energies higher than 10 keV. The cut-off is then determined by the electron temperature: when $E_{phot} \sim kT_c$ the energy transfer is no longer efficient and the process stops, producing the observed decrease at $\sim 100 - 200$ keV.

- Assuming an isotropic emission from the corona, about half of the light is radiated towards the observer and about half towards the disk. The interaction of high-energy photons with this colder, optically thick material happens via absorption, reflection and fluorescence. This process is referred to as Compton Reflection. Qualitatively, X photons of energies in range $\sim 1 - 100$ keV impact on the disk and produce a reflection continuum directed towards the observer, added up to the corona's continuum (the power law). The reflection component shows various emission and/or absorption features, which contain informations about the accreting material, as detailed below.

1.3.1 Emission lines

The incidence of the radiation from the corona on the accretion disk produces a reflection continuum and fluorescence lines of the most abundant elements. The most prominent lines are produced by iron (Fe), but the same arguments detailed below apply to all elements.

Fe K lines are originated when the absorption of an X-ray photon with an energy above the threshold of 7.1 keV (iron edge) causes the ejection of one of the two electrons in the K-shell, ionizing the atom. The electronic configuration is in an excited state and the subsequent redistribution can happen in two ways. In one case, an electron from the L-shell transits in the K-shell, releasing a photon at energy 6.4 keV that has a 34% probability of exiting the atom; in such a case, this photon contributes to the Kα line. In the remaining 66% of the cases, the photon is absorbed internally by another electron, which is, in turn, ejected from the atom (Auger effect). The second possibility is that the electronic transition is from the M-shell to the K-shell, producing a photon at an energy of 7.05 keV thaw we associate with the iron Kβ line.

The above considerations are valid when the iron atom is neutral. At higher ionization states, the energies increase accordingly. In particular the Kα line can reach 6.97 keV for H-like iron (Makishima, 1986) (Fig.1.3). The energy of the fluorescence line observed in AGN is typically 6.4 keV rest-frame (Mushotzky et al., 1993). This value is consistent with the hypothesis of reflection from cold, neutral material with low velocity, in the disk or in the molecular torus.

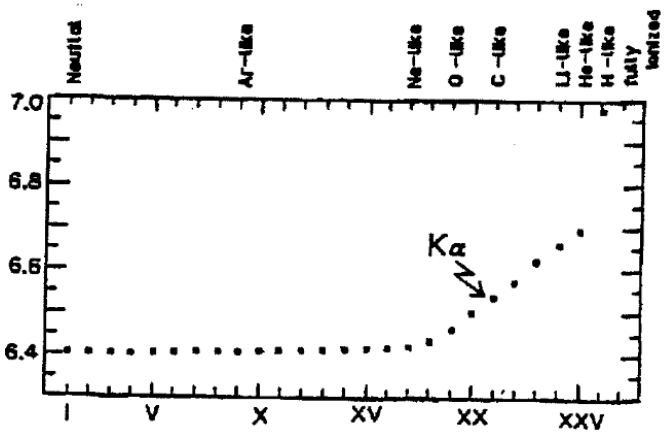

Figure 1.3: Ionization states of the Fe atom vs. energy expressed in keV. The points show the increase of the energy of the Fe Kα fluorescence line at increasing ionization levels. Credit: Makishima (1986).

The strength of the line with respect to the continuum is measured by the equivalent width (EW). In Seyfert 1 galaxies the Fe Kα EW spans in

the range 50–350 eV, being typically of ∼150 eV.

An emission line is intrinsically narrow and can be broadened by several effects, for example thermal agitation or collisions. In the Compton reflection model it is assumed that the emitting material is the rotating accretion disk, located in the proximity of the SMBH: in this case the principal distorting effects on the line are due to orbital motion and Relativity. The combination of these factors can then induce a strong profile deformation, as described in the following:

- Classic Doppler effect, due to the motion around the black hole, causing an energy shift. This can be expressed as $E_{obs} = E_{em}(1 \pm \beta)$, where E_{obs} is the measured energy, E_{em} is the emission energy, $\beta = |v|/c$. This effect, depending on the relative velocity between the material and the observer, causes a double-peaked profile, where the receding gas produces the red peak and gas moving toward the observer produces the blue peak (first panel in Fig.1.4). An estimate of the broadening can be derived as follows: matching the centripetal and gravitational forces, $\frac{v^2}{r} = \frac{GM_{BH}}{r^2}$, it is possible to find a relation between the velocity and the distance r from the center of a Keplerian orbit: $\beta^2 = r_s/2r$, being $r_s = 2GM_{BH}/c^2$ the Schwarzschild radius. Using this β in the Doppler effect equation we find:

$$\Delta E = E_{blue} - E_{red} = E_{em}(1+\beta) - E_{em}(1-\beta) = 2E_{em}\beta \propto (r_s/r)^{1/2} \tag{1.9}$$

- The rotational velocity of the accretion disk for an annulus with radius $r \gtrsim r_s$ can be estimated as the velocity of a Keplerian circular orbit: $v \sim (GM_{BH}/r)^{1/2}$, so $\beta \propto (r_s/r)^{1/2}$. In the inner regions, velocities are higher and relativistic effects no more negligible. In Special Relativity the Doppler effect equation can be written as $E_{obs} \simeq E_{em}\sqrt{\frac{1 \pm \beta}{1+\beta}}$. The line profile is deformed by relativistic beaming, which boosts the blue peak and decreases the red one. The transversal Doppler effect, $E_{obs} \simeq E_{em}\sqrt{1-\beta^2}$, shifts the whole structure at lower energies (second panel in Fig.1.4).

- When the accreting matter reaches the inner regions ($r \leq 10 r_g$) General Relativity effects become important. Gravitational redshift induces a global shift to lower energies, which is larger at smaller distances: $\nu_{obs} = \nu\,(1 - r_s/r)^{1/2}$ (third panel in Fig.1.4).

All these effects act on the matter producing Fe photons and the dominant effect is determined by the distance from the SMBH. The overall shape

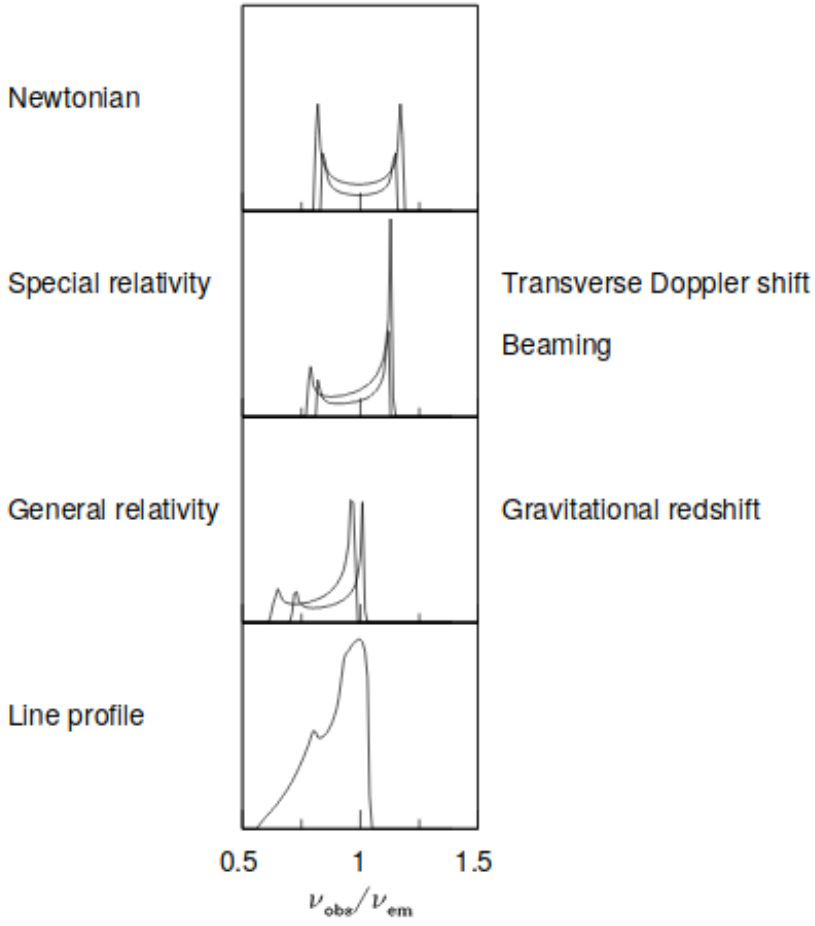

Figure 1.4: Deformations of the Fe Kα line shape in AGN spectra due to different effects: in the first panel Doppler shifting due to the rotation; in the second panel, the beaming of the blue-shifted peak and the decrease of the red-shifted one due to special relativity; in the third panel the global shift at lower energies due to general relativity; in the fourth panel the final profile obtained summing all the effects and integrating on the radius of the disk region where the line is emitted. Credit: Fabian et al. (2000).

of the emitted Fe lines is obtained by integrating from the the internal radius, r_{int}, to the end of the disk, r_{end}. By doing so, we obtain the broadened and asymmetric profile shown in the last panel of Fig. 1.4.

Many parameters of the disk and the disk-observer system can affect the resulting line shape: the inclination, the internal and external integration radii, the emissivity of each annulus, the ionization state, the density profile, etc. Grossly speaking, however, the extent of the red peak depends on the distance of the innermost part of the disk from the SMBH. In case of a non-rotating black hole the spacetime metric is described by the Schwarzchild metric and the innermost stable orbit is at 6 r_g, while for a rotating one in a Kerr metric, the inner radius is located at 1.25 r_g. The line profiles (shown in the left panel of Fig. 1.5) are different in the two cases, since in presence of a Kerr black hole the profile reaches lower energies. In principle and for a limited number of AGN in the local Universe, these differences in the observed AGN line profiles can be used to infer the spin of the SMBH when compared to models.

The extent of the blue peak is mainly due to the inclination: the line stretches blue-ward when the angle increases, as seen in the right panel of Fig. 1.5.

1.3.2 Absorption

Several Seyfert 1 and RQ AGN show evidence for absorption features in the range $\sim 4 - 10$ keV. They are interpreted as Doppler shifted resonant absorption lines due to highly ionized (H-like, He-like) iron (Cappi, 2006).

In the energy range 4–6 keV these lines are red-shifted and are most likely due to infalling flows with velocities up to 0.1–0.4 c, column densities $\gtrsim 10^{22}$ cm^{-2} and very large ionization parameters (ξ $\sim$1000 erg s^{-1} cm) (Dadina et al., 2005). An example is shown in Fig.1.6.

Absorption Fe features blue-shifted at energies above 7 keV are due to gas moving outwards. Outflows are quite common in AGN and have been studied since a long time (see, e.g., the spectra of broad absorption line (BAL) QSO, and the Warm Absorbers observed in the soft X-ray band). The most extreme outflows show velocities up to $\sim 0.2 - 0.4$ c, high ionization, $\log(\xi) \sim 3 - 6$, and column densities as large as $N_H \simeq 10^{22} - 10^{24}$ cm^{-2}. They are defined Ultra Fast Outflows (UFOs) (Tombesi et al., 2010). An example of absorption due to a UFO is shown in Fig. 1.7.

They are expected to have a significant role in the evolution of the host galaxy, such as the enrichment of the ISM and the reduction (or suppression) of the star formation. They can also explain some fundamental relations between the host galaxy and the SMBH. The ejection of a huge amount of mass from the central regions of AGN can also inhibit the growth of the SMBHs, potentially affecting their evolution. The study of UFOs provides

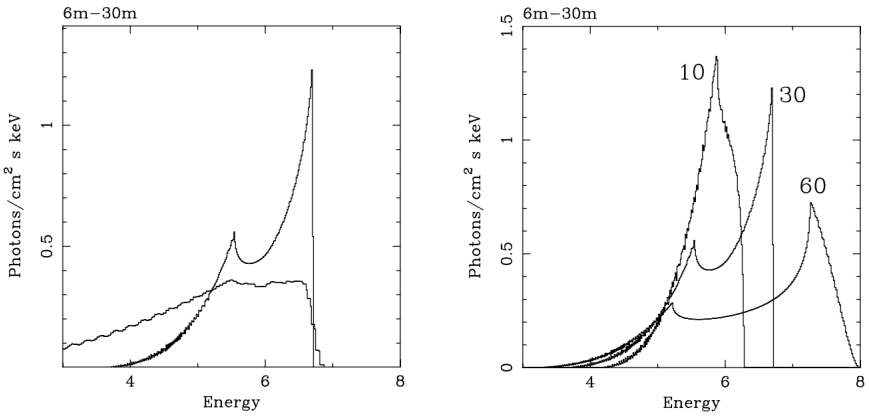

Figure 1.5: On the left panel: comparison of relativistic iron line profiles from an accretion disk around a Schwarzschild black hole (narrower, peaky line) and a near-extremal Kerr black hole (broader line). The line emission is assumed to extend down to the radius of marginal stability which is $6r_g$ and $1.25r_g$, respectively. The difference in the width and redshift of the line is principally a result of the difference in the position of the radius of marginal stability. On the right panel: relativistic iron line profiles for the case of an accretion disk around a Schwarzschild (non-rotating) black hole. It is assumed that the region of the disk producing fluorescence extends from $6r_g$ to $30r_g$. Three inclination angles for the disk are shown: 10°, 30°, and 60°. The main effect of increasing the inclination is to broaden the line by increasing its high-energy extent. Credit: Fabian et al. (2000).

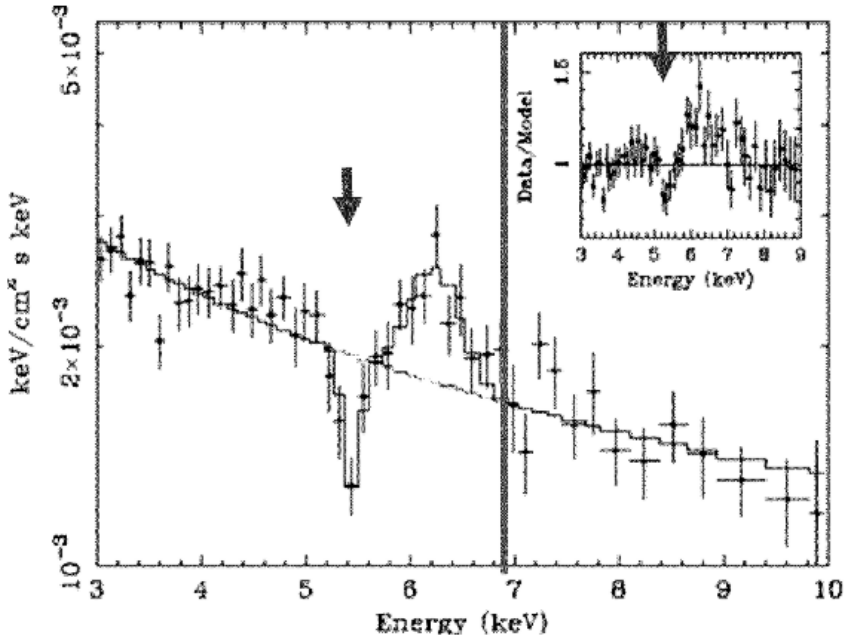

Figure 1.6: BeppoSAX unfolded spectrum of Mrk 509 showing the absorption structure (indicated by the arrow) redward of the Fe K emission line visible at ∼6.2 keV. The energy at 6.9 keV, corresponding to H-like Fe, is marked by a vertical line. Credit: Dadina et al. (2005), Cappi (2006).

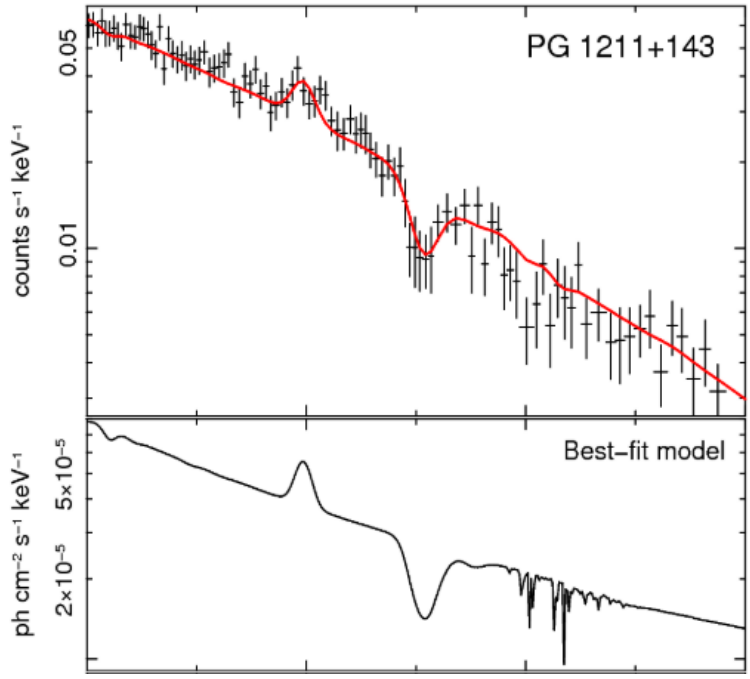

Figure 1.7: XMM-Newton EPIC pn spectrum of PG 1211+143 in the 4—10 keV band, in which a UFO with v∼0.15 c has been detected. Upper panel: background-subtracted source spectrum with superimposed the best-fit model. Lower panel: best-fit model. Credit: Tombesi et al. (2010).

also important insights on how the AGN works and on the black hole accretion/ejection physics in general.

1.4 Variability

AGN display erratic, aperiodic flux variability over a wide range of timescales (from years to minutes) (Padovani et al., 2017). The main property of AGN variability is its "red noise" character, namely the occurrence of larger amplitude variations on longer timescales.

Much faster variability is observed in the X-ray band than in any other. In Fig. 1.8 an example of the X-ray light curve of the Seyfert 1 galaxy NGC 3783 is shown.

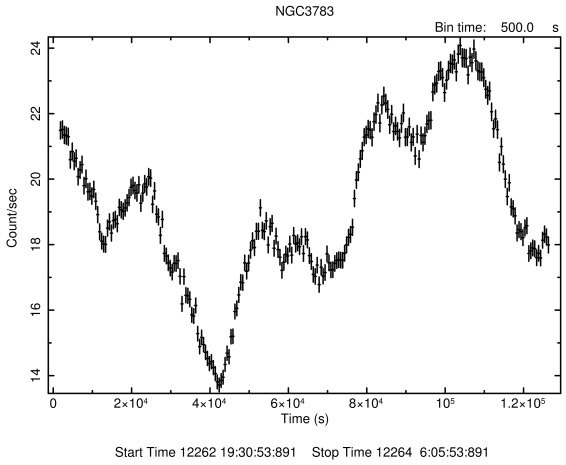

Figure 1.8: Light-curves of NGC 3783 (rev. 372) in the energy band 0.3–10.0 keV; every time bin has 500s-length. We see a variation of almost a factor if 2, from ∼13 to∼24 counts/s, on time scales as short as ∼50 ks.

The minimum timescale of variability measured in a given waveband allows us to infer an upper limit for the size of the emitting region. By imposing R$\leqslant \Delta$t c, we find the most rapidly varying regions (t_{var} ∼ few 10 ks) to have sizes smaller than ∼ 10^{15} cm∼ 10^{-3} pc (Mushotzky et al., 1993). This short variability is thought to originate in the innermost regions of the accretion flow (corona and inner disk). Moreover, it is responsible for driving (at least part of) the variability from the outer accretion disk, observed at longer wavelengths (UV and optical) and over longer periods. Observing diverse timescales for variability in distinct parts of the spectrum can help us to distinguish separate processes in act and understand where they are possibly originated.

In this regard, the variability of the Fe Kα lines is particular interesting,

because from the time evolution of their profile we can recognize directly changes due to motions or modifications of the emitting material in the very central regions. For example, infer on the geometry and dynamics at small distances from the black hole we can test variations in the Fe Kα line originated by orbital motions, analyzing the time scale of the Keplerian orbital period at a distance of 10 r_g, where $r_g = GM_{BH}/c^2$. It is estimated by Bardeen et al. (1972):

$$T_{orb} = 310 \left[a + \left(\frac{r}{r_g} \right)^{3/2} \right] M_7 \quad s \tag{1.10}$$

where a is the black hole spin: $a = 0$ corresponds to a non-rotating black hole, with the surrounding spacetime being described by the Schwarzschild metric, whereas for a maximum rotating black hole with $a = 1$ the Kerr metric is used. M_7 is the SMBH mass expressed in units of 10^7 $M_\odot$. The masses of the black holes in AGN typically span in an interval of $10^6 - 10^9$ $M_\odot$. For a medium value of $\sim 10^7$ $M_\odot$ we find $T_{orb} \sim 10$ ks.

A practical way to analyze the temporal evolution of this emission feature is the Excess Maps technique, introduced in Iwasawa et al. (2004) and later used in Turner et al. (2006), Tombesi et al. (2007) and De Marco et al. (2009). This time-resolved spectral analysis is based on the representation of excess residuals against a spectral continuum in the time-energy domain. This method allowed Iwasawa et al. (2004) to spot sinusoidal variations of the excess in band 5.7-6.2 keV with a period of ∼25 ks for the Seyfert 1 galaxy NGC 3516, shown in Fig. 1.9. These results were interpreted as Doppler modulations of a Fe Kα line broadened by gravitational redshift. Studying its profile it was possible to place constraints on the emitting region, limiting it to the range of 7-16 r_g, thus allowing an estimate of the black mass of $(1 - 5) \times 10^7$ $M_\odot$.

Using the same method, Turner et al. (2006) found in Mrk 766 a modulation in the Fe Kα emission with period of ∼165 ks, interpreted as due to orbiting material at distance $\lesssim$100 r_g from the black hole, as shown in Fig. 1.10.

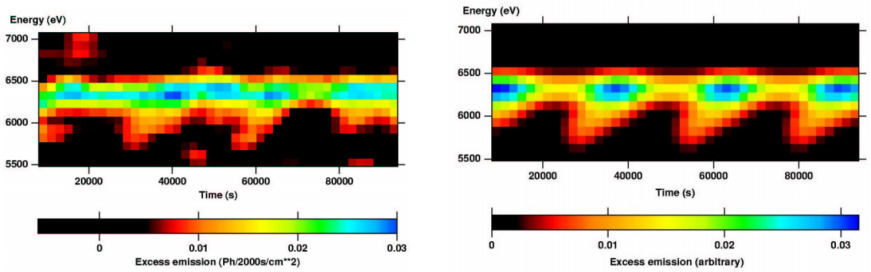

Figure 1.9: Left panel: excess map obtained from a XMM-*Newton* observation of NGC 3516, in which there are recurrent red-ward features. Right panel: a simulated excess map replicating the emission of a flare rotating above the disk: this represents a possible explanation for the data. Credit: Iwasawa et al. (2004).

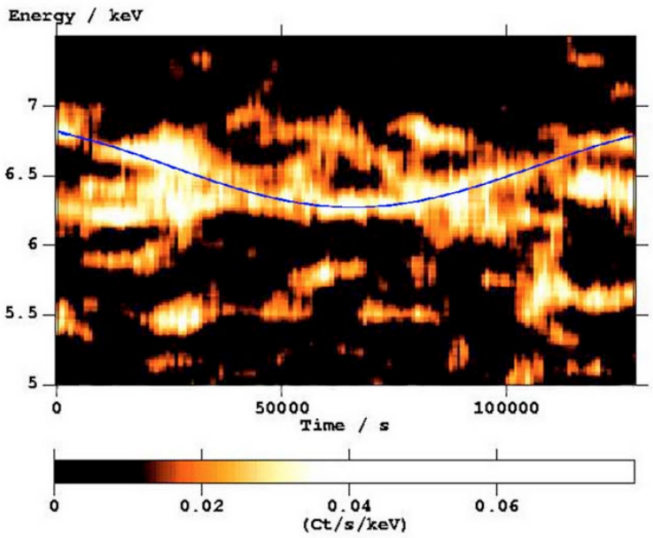

Figure 1.10: Smoothed excess map obtained by a XMM-*Newton* observation of Mrk 766. The blue line follows the periodic energy-shift of the Fe Kα peak. Credit: Turner et al. (2006).

Chapter 2

Residual maps

The main goal of this Master Thesis is to identify variable features in the Fe K line energy band and to analyze their variability pattern in detail, to potentially infer information on accreting/outflowing material kinematics and dynamics. The features we are searching for may not appear at fixed and/or a-priori known energies, so basic time-resolved spectral analysis techniques of spectral fitting with template models are not always convenient for our purposes. Therefore we used a technique based on inspecting residuals above and below the given continuum in time-energy domain (as explained in Sect. 2.1). This method is based on the *Excess Map technique* that we introduced in Section 1.4, down to very short time scales.

The Excess Maps technique consists in calculating residuals to the continuum best-fit model in short-duration spectra and visualizing them on an image in the time-energy domain. The basic idea behind this method is that the X-ray spectra of RQ-AGN in the 2–10 keV band are well described by simple models, usually a power law, and that all the residuals above this model represent discrete Fe emission lines and all the residuals below are due to discrete Fe absorption features.

While the authors who already used this technique chose to analyze only positive residuals (therefore the *excess* map denomination), we study here simultaneously all wresiduals, both positive and negative, hence we name these maps as *residual maps*.

Variability patterns in absorption and emission can help us probing and separating all physics phenomena involved; the comparison of emission vs. absorption components bring potentially new physical information. In fact, absorption and emission components could show some kind of correlation, pointing to an interconnection between the motions of emitting and absorbing material. Finding a link between emission from the disk and absorption from the outflows could help understanding the mechanism that produces the latter, which is still an open question. In this regard, my

Master Thesis work is meant as a first, preliminary but fundamental step to shed light on the innermost regions of accreting SMBHs via analysis of emission/absorption features using the *residual maps* technique.

2.1 Method

Here I present an outline of the adopted method:

- Time and energy bins, Δt and ΔE, are chosen following the discussion provided in Sections 2.1.1 and 2.1.2.
- Spectra of a duration Δt are extracted in sequence from each observation and corrected for the corresponding background by subtraction. Each spectrum is binned adopting the fixed ΔE.
- A continuum model is fitted to each spectrum, in general in the bands 4.0 – 5.0 keV and 7.0 – 10.0 keV (see Sections 4.2 and 5.2 for the specific intervals chosen for the sources investigated here). The 5.0 – 7.0 keV range is excluded at first in the fit because of the presence of the Fe Kα line, which would obviously introduce an error in the modeling of the continuum. The basic model includes a power law and a cold absorption component (`power law` and `phabs` on *Xspec*). The latter is needed to account for a possible residual curvature produced by warm absorbers, which could still be detectable above $\sim$ 4 keV.
- The fit model is subtracted to the whole 4.0 – 9.0 keV band data, and the data− model residuals are first expressed in counts s^{-1}.
- Residuals are divided by the effective area of the detector to correct for the instrumental response, so they are finally expressed in counts s^{-1} keV^{-1}.
- This procedure is applied for each time interval of a single observation, and the resulting residuals are put together and displayed in a map of the time-energy plane.
- A similar map is constructed using $\Delta\chi$, which gives an immediate estimate of the significance of the possible features. $\Delta\chi$ is dimensionless, as it is defined as

$$\Delta\chi \;=\; \frac{data - model}{standard\ deviation} \tag{2.1}$$

2.1.1 Time resolution

The choice of the time resolution depends on the physical phenomenon that produces the variability.

Once it is decided which phenomenon to study and once the time-scale t_{ts} on which it is supposed to vary is computed, we can choose a time resolution Δt. Following the Nyquist-Shannon oversample theorem, it must satisfy $\Delta t = t_{ts}/2\beta$, with $\beta \geq 1$, in order to properly sample, i.e. oversample, the characteristic time scale.

With real data, however, the choice of the time resolution is limited by photon statistics: in each time-energy pixel we must have a minimum of $\sim$20 counts to apply the χ^2 statistics. Choosing sources with the highest possible flux allows us to analyze short-term variability, while to study longer time-scales, sources with lower flux are sufficient.

2.1.2 Energy resolution

The Fe Kα line profile is described in Section 1.3.1. The best way to analyze its temporal evolution at a given distance from the SMBH is to choose an energy resolution as small as the detector spectral resolution in the analyzed band. Using EPIC pn data in the 4–10 keV energy range implies Δ E=0.1 keV (see Table 3.1), although there is not a good oversampling of narrow features.

2.2 How to read a residual map

In Fig. 2.1 we show an example of a residual map. In particular, this is related to the observation 372 of NGC 3783 (further details on the data will be given in Chapter 4).

On the x-axis we have the time bins: each of them represents a time interval equal to the chosen time resolution Δt. On the y-axis we have the energy, sectioned by the chosen ΔE. In 2.1 Δt is 2.5 ks and ΔE is 100 eV.

In this way, every horizontal line shows the time-evolution of the residuals at a fixed energy, while every vertical line represent the residual spectrum in the total bandwidth at a fixed time.

As we can see from the color-bar, different colors indicate the intensity of the excess (in red) and of the absorption (in blue).

A way to highlight the features and to locate them more easily is to apply a Gaussian filter to the image, as we can see in Fig. 2.2. Visualizing the data in a smoothed map allows us to immediately pinpoint regions of interest that we can then study thoroughly via spectral analysis.

In the example map we see that the darkest pixel are concentrated in a horizontal line at E$\sim$6.3 keV: it represent the Fe Kα line, affected by cosmological redshift. The emission line is always present above the continuum, for the whole observation.

Right above we see some blue features; they do not appear as a constant line but as spots of different intensity and indicate the presence of a variable

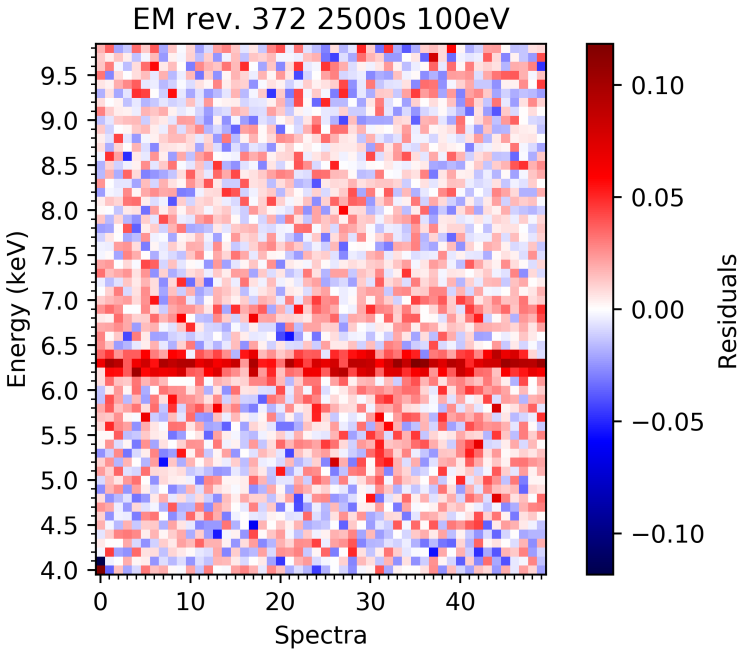

Figure 2.1: An example of a residual map, in particular that produced using the observation 372 of the Seyfert 1 galaxy NGC 3783. On the x-axis we show the spectra extracted in sequence, each of duration of 2.5 ks: they are used as an indication of time. On the y-axis we plot the energy expressed in keV, with a resolution of 0.1 keV. The colors represent the intensity of the residuals: positive residuals are shown in red, while negative ones are in blue.

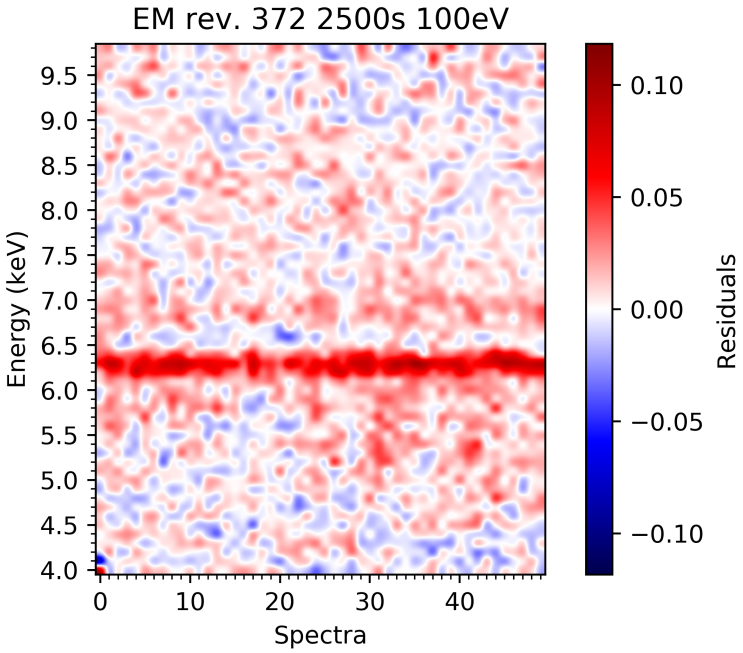

Figure 2.2: An example of a smoothed residual map, produced from the observation 372 of the Seyfert 1 galaxy NGC 3783. A Gaussian filter is applied to the image to highlight the small-scale features.

absorption at energies compatible with a mildly blue-shifted Fe Kα; further analysis is clearly needed to understand whether they can be ascribed to an outflow.

At even higher energies ($\sim$6.9 keV) we can recognize a second, broader, emission line: this one does not appear to be constant as the first we identified; in fact, in the first half of the observation it appears as patchy, while in the second half it seems stable. From the energy range it is compatible with either a Fe Kβ line or a ionized Fe Kα.

At energies redward of the Kα we see complex emission structures: they could represent the red wing of the line, broadened by effects described in Sect. 1.3.1. Their shapes change throughout the whole observation; in particular, they extend to much lower energies in the final part of the observation and they seem to be at least partially absorbed between spectra 15 and 20.

As stated in Section 2.1, we can also produce maps of $\Delta\chi$ instead of residuals, as shown in Fig. 2.3. They provide an immediate idea of the significance of a given feature. It is to be noted, though, that this is a lower limit and that is due to the small time and energy resolution we are using, which grant us only a limited number of counts.

For example, if we see a long-lasting, low-significance structure in the map (so, a horizontal spot with a low saturated color) we can carry our detailed analysis on the spectrum extracted from the time identified with the start of the spot to its end. Integrating over a longer time we accumulate a higher number of counts, and the feature can be detected with a higher significance.

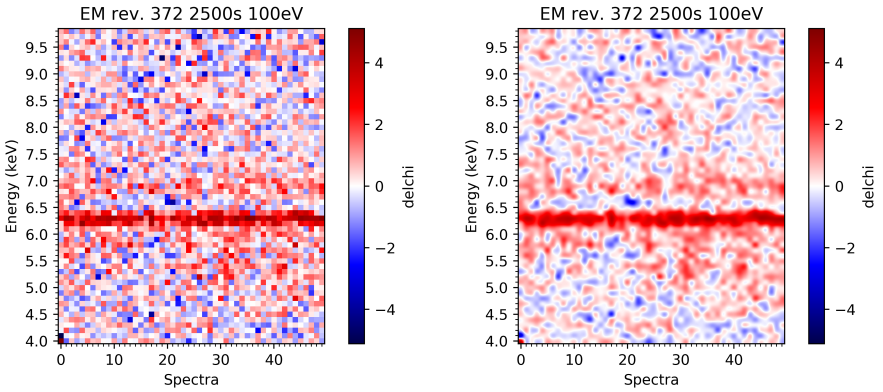

Figure 2.3: Residual maps of the observation 372 of NGC 3783, normal (left panel) and with a Gaussian filter applied (right panel). The colors in this case represent the intensity of $\Delta\chi$, which is a direct indication of the significance of the features.

In every map, the two pixels on the bottom left are modified. We found the minimum and the maximum values among all residuals of each map, and took the highest absolute value between them. We put this value on the first and second pixels of the first spectrum, in positive and negative, respectively. This has been done in order to have a "symmetrical" color bar: if the highest and the lowest values are the same, the pixels with a value $\sim$0 (i.e. those that do not represent any emission/absorption feature and are a good match with the continuum) appear white, while all excesses are in shades of red and all absorptions in shades of blue. We make the substitution in that particular position because we do not expect to see significant deviations from zero in the bands where we fit the continuum. However, we use these modified maps only for visualization purposes, and used the "real" data for the tests that we will describe in Chapter 7.

Chapter 3

XMM-*Newton* and source sample selection

As described in Chapter 2, the residual map technique consists in splitting the source observations in small time and energy intervals and studying the residuals obtained modeling the underlying continuum. In order to probe emission/absorption lines variability on the shortest possible time-scales, it is necessary to use data with the highest possible number of counts, in order to have significant photon statistics in each pixel of the "time-energy" plane. The most suitable X-ray mission for this purpose is the X-ray Multi-Mirror Mission (XMM-*Newton*) which provides the highest possible sensitivity (i.e. signal to noise ratio, SNR) at the energies close to Fe K band.

3.1 The telescopes

XMM-*Newton* is the ESA cornerstone X-ray observatory, launched in December 1999. On-board there are three X-ray telescopes, each composed of 58 gold-coated shells, nested in a co-axial and co-focal Wolter I configuration (Fig.3.2). Each shell consists of a paraboloid and an associated hyperboloid grazing incidence mirror. This configuration is necessary to reflect high-energy radiation: on a material with density ρ, photons are reflected if the incidence angle is lower than a critical angle $\theta_{crit} \propto \sqrt{\rho}/E$. The focusing optics grant a good angular resolution: the Point Spread Function (PSF, the distribution on the focal plane of a point-like source) has a Full Width at Half Maximum (FWHM) of ~ 6" at the center of the Field of View, and Half Energy Width (HEW, the PSF diameter that includes 50% ot the total energy of the source) of ~ 15", since the PSF has not a Gaussian shape (see Fig. 3.1).

There is also an optical/UV telescope, used to observe counterparts of the X-ray sources.

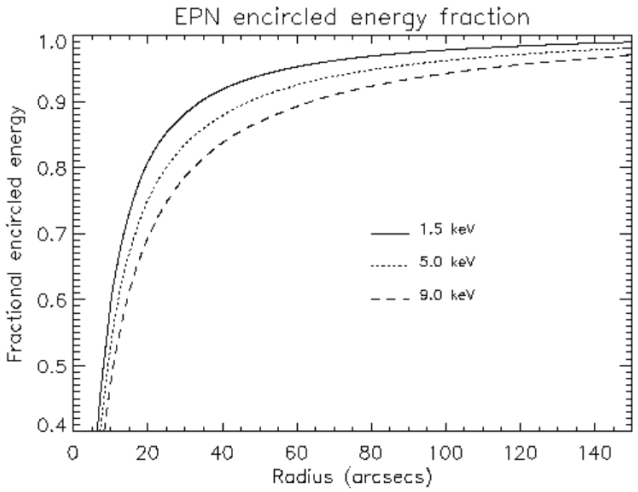

Figure 3.1: The pn fractional encircled energy as a function of the spectral extraction radius at different energies. This plot shows what is the fraction of photons contained in a given extraction radius for a point-like source at a given energy. The curves are calculated integrating the PSF. Credit: ESA's XMM-*Newton* Users Handbook.

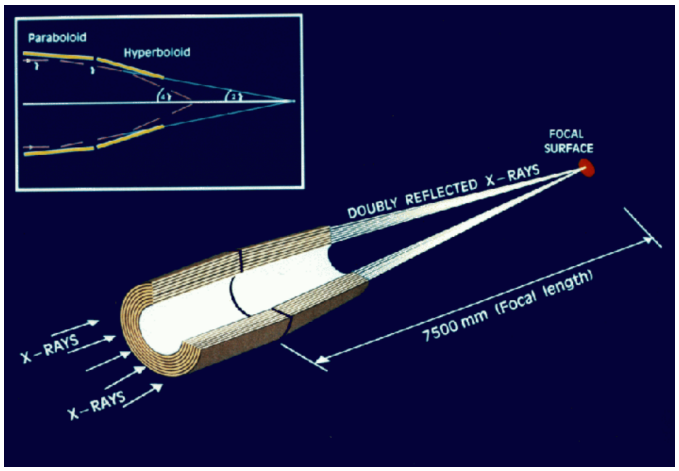

Figure 3.2: Light path in the XMM-*Newton* telescope with EPIC pn camera in its primary focus. The grazing incidence optics are in Wolter I configuration. The double reflection, first on a paraboloid and then a hyperboloid surface, optimizes the collection of high-energy photons. Credit: ESA's XMM-*Newton* Users Handbook.

3.2 The on-board instruments

The three main scientific instruments on-board XMM-*Newton* (see Table 3.1) are:

- The European Photon Imaging Camera (EPIC): three CCD cameras, *pn*, *MOS 1* and *MOS 2*, each on the focal plane of one of the three X-ray telescopes. The EPIC CCDs produce images and offer medium-quality spectroscopy, with a resolving power E/Δ E $\sim$ 20-50; around the Fe Kα line (E $\simeq$ 6.4 keV) this corresponds to a spectral resolution of $\sim$ 150 eV.
- The Reflection Grating Spectrometer (RGS): two identical spectrometers, which grant an excellent spectral resolution, with $E/\Delta E \sim 200-800$, for energies from $\sim$ 0.3 keV up to 2.5 keV. They are mounted on the same telescopes of the MOS: the incident light is split by a grating (*RGA*): $\sim$ 40% of the photons are diverted towards the RGS and $\sim$ 44% reach the MOS directly, while a small fraction is lost.
- The Optical Monitor (OM): it produces optical and UV images and spectra in different filters between 170 nm and 650 nm.

Instrument	**EPIC pn**	**EPIC MOS**	**RGS**	**OM**
Bandwidth	0.15 - 15 keV	0.15 - 12 keV	0.35 - 2.5 keV	180 - 600 nm
Sensitivity [a]	$\sim 10^{-14}$	$\sim 10^{-14}$	$\sim 8 \times 10^{-5}$	20.7
Field of view	30'	30'	$\sim$ 5'	17'
FWHM	6"	5"	5"	1.4"-1.9"
HEW	15"	14"	14"	-
Pixel	150 μm (4.1")	40 μm (1.1")	81 μm	$\sim$0.48"
Time resolution [b]	0.03 ms	1.5 ms	16 ms	0.5 s
Spectral resolution	$\sim$ 80 eV [c]	$\sim$70 eV	0.04/0.025 Å [d]	350 [e]

Table 3.1: Technical characteristics of the detectors on XMM-*Newton*.
(a) Expressed in erg s^{-1} cm^{-2} for pn, MOS and RGS.
(b) In timing mode for EPIC, high time-resolution model for RGS and fast mode for OM (the fastest data acquiring modality for each detector).
(c) At 1 keV, it becomes 150 eV at 6.4 keV for both EPIC cameras.
(d) 3.2 eV at 1 keV.
(e) Resolving power expressed as $\lambda/\Delta\lambda$.
Data from ESA's XMM-*Newton* Users Handbook.

In Fig. 3.3 the effective areas of the three EPIC instruments are shown, compared to the two *ACIS* (Advanced CCD Imaging Spectrometer) onboard NASA's *Chandra X-ray Observatory*: we note that XMM-*Newton* sensitivity is considerably higher at all energies. In particular, the pn camera has the

highest response, reaching a maximum of $\sim$ 1270 cm^2 at E $\simeq$ 1.5 keV and about 700-800 cm^2 in the Fe K energy band (E$\sim$ 6-7 keV). The EPIC MOS cannot achieve such a high sensitivity, not even if MOS 1 and 2 are added together: this is to be ascribed to the partition of the light with the RGS spectrometers.

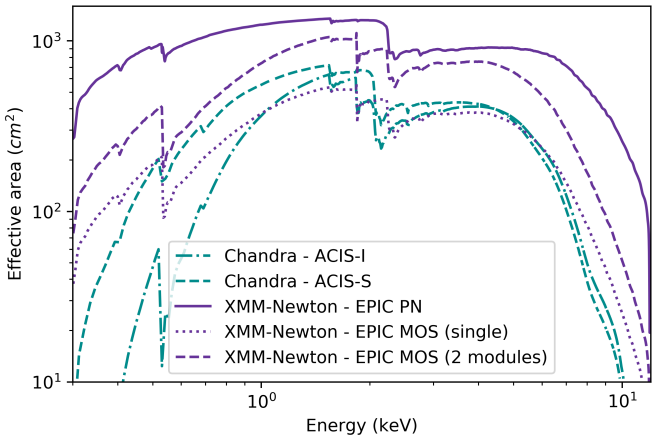

Figure 3.3: Comparison of the effective areas of instruments onboard *Chandra* and XMM-*Newton*. The pn instrument onboard XMM-*Newton* is the most suitable for the kind of investigation described in this thesis, since it guarantees the collection of a large number of counts up to high energies, including the iron line spectral interval.

All the instruments on XMM-*Newton* work simultaneously and autonomously. Each instrument can be programmed with different settings in order to optimize the observations for the needed scientific aim.

Thanks to its high eccentricity elliptical orbit, uninterrupted pointings up to $\sim$ 130 ks ($\sim$ 36 h) can be carried out, allowing variability studies and monitorings to be performed efficiently.

The unique sensitivity in Fe band and the possibility to obtain long monitoring programs make XMM-*Newton* pn the most suitable instrument for the study proposed in this thesis.

RGS are ideal for spectral analysis, but they do not cover our range of interest and, because of their limited effective area, they do not allow to collect a sufficient number of photons for our purposes.

3.3 The 3XMM-DR7 catalogue

The 3XMM-DR7 catalogue (Rosen et al., 2016) was released in June 2017. It contains source detections drawn from 9710 XMM-*Newton* EPIC observations carried out between 2000 February 3 and 2016 December 15, and all the datasets that were publicly available by 2016 December 31. It covers

an energy range from 0.2 keV to 12 keV, divided in several energy bands, as shown in Table 3.2).

Basic energy bands	**1**	0.2 - 0.5 keV
	2	0.5 - 1.0 keV
	3	1.0 - 2.0 keV
	4	2.0 - 4.5 keV
	5	4.5 - 12.0 keV
Broad energy bands	**6**	0.2 - 2.0 keV
	7	2.0 - 12.0 keV
	8	0.2 - 12.0 keV
	9	0.5 - 4.5 keV

Table 3.2: Energy bands used in the 3XMM-DR7 catalogue.

Net exposure times in these observations range from <1 up to ∼130 ks (that is, a full orbit of the satellite).

The total sky area of the catalogue observations with effective exposure >1 ks is ∼1750 deg^2, which translates into ∼1032 deg^2 when corrected for field overlaps.

The catalogue contains 727790 X-ray detections; of these, 499266 are unique X-ray sources. 94269 X-ray sources have multiple detections in separate observations (up to 50 observations), thus allowing first-order variability studies.

Each source in the catalogue is reported with 332 columns which include all the relevant information about the source (position, number of counts and fluxes in different energy band, significance of the detection, variability) and details about the observation (e.g., length of the exposure, adopted filters, etc.).

3.4 Source sample selection criteria

Local, bright Seyfert 1 galaxies are the proposed targets for this work, since their low/absent cold obscuration (typically, $N_H \leq 10^{22}$ cm^{-2}) and large number of counts per second offer the "cleanest" and "direct" view to probe the properties of AGN inner flows. Furthermore, they are radio-quiet AGN, so their X-ray spectra are likely not contaminated by the presence of jets and their Doppler boosted emission.

The first criterion to select the objects to which apply the residual map technique is thus the highest possible X-ray flux. From the 3XMM-DR7 catalogue (Sect. 3.3) we searched for all AGN observed by EPIC pn and with a flux larger than 5×10^{-12} erg s^{-1} in band 5 ($4.5 - 12$ keV), i.e. the

one that covers the energy range of the Fe Kα line at 6.4 keV. The mean flux for each target is calculated among the values of the various observations included in the catalogue. Among the flux-selected sources, we searched for those with the longest individual observations provided by the catalogue and the longest total exposure times, to follow variability on different time-scales.The selected candidates are listed in Table 3.3.

Source	**Object Type**	**Exposure Time** ks	**Mean flux 4.5-12 keV** erg $s^{-1}cm^{-2}$
NGC 3783	Seyfert 1	453	3.34×10^{-11}
Mrk 509	Seyfert 1	834	3.08×10^{-11}
MGC -06-30-15	Seyfert 1	542	2.93×10^{-11}
MR 2251-178	QSO RQ Type 1	527	2.72×10^{-11}
NGC 5548	Seyfert 1	746	2.46×10^{-11}
Ark 120	Seyfert 1	599	2.44×10^{-11}
SWIFT J2127.4+5654	Seyfert 1	421	2.22×10^{-11}
NGC 4051	Seyfert 1	418	1.27×10^{-11}
Ark 564	NL Seyfert 1	492	1.12×10^{-11}
Mrk 766	Seyfert 1	421	9.11×10^{-12}

Table 3.3: List of the selected sources from the 3XMM-DR7 catalogue, reported at decreasing fluxes in the $4.5 - 12$ keV band.

To fully exploit the timing capability of the technique applied here we also added to the candidate list the two galaxies with the longest total exposures provided by the catalogue, even though their flux is about one order of magnitude below the adopted limit, as seen in Table 3.4.

Source	**Object Type**	**Exposure Time** ks	**Mean flux 4.5 - 12 keV** erg $s^{-1}cm^{-2}$
IRAS 13224-3809	Seyfert 1	2076	3.80×10^{-13}
1H0707-495	NL Seyfert 1	1030	5.35×10^{-13}

Table 3.4: List of the selected sources with the longest total exposures from the 3XMM-DR7 catalogue, reported at decreasing fluxes in the $4.5 - 12$ keV band.

3.4.1 Selected sources

We finally decided to focus our analysis on the following sources: NGC 3783, Mrk 509 and IRAS 13224-3809. The first two sources were chosen because they are the brightest objects in our sample, while the third one was selected because it has the longest exposure of all XMM-*Newton* observations as detailed below. More information on these sources can be found in the

respective chapters: 4, 5 and 6.

NGC 3783: It is the brightest AGN of our sample in the energy band of our interest. Observations from 2000 and 2001 of this source were already analyzed with the excess mapping technique (Tombesi et al., 2007), so it is also ideal to make a comparison between the results of our updated (and improved) procedure and what was found and published earlier.

In 2016 it has been monitored by *Swift* to track the X-ray hardness variability (i.e., to see the most significant X-ray spectral changes). In December, it showed evidence for an intense obscuration event which triggered new XMM-*Newton* observations. An obscurer was found to partially cover the central source. It was highly ionized, with a column density of few 10^{23} cm^{-2} and a velocity of few 10^3 km s^{-1}, being responsible for the Fe XXV and Fe XXVI absorption lines detected in the spectrum (Mehdipour et al., 2017).

Mrk 509: It has the second highest flux of our source list. Its spectrum shows several absorption features consistent with H-like iron lines, associated with an outflow with mildly relativistic velocity. These lines appear to be variable in energy and intensity on time-scales as short as ∼20 ks, implying variations in the column density, geometry and/or ionization structure of the outflow (Dadina et al., 2005; Cappi et al., 2009).

IRAS 13224-3809: This source was observed for a long and, in particular, with a continuous campaign of 1.5 Ms in summer 2016. The inclusion of the old datasets provides a total exposure that exceeds 2 Ms. The latest observations indicate the presence of an Ultra Fast Outflow with a velocity of ∼0.2 c, that strongly anti-correlates with the emission from the inner accretion disk (Parker et al., 2017).

Chapter 4

NGC 3783

NGC 3783 is a Seyfert 1 galaxy at redshift $z = 0.0097$. The SMBH has a mass of $M = 3.0 \pm 0.5 \times 10^7$ $M_\odot$, estimated by reverberation mapping studies in optical and UV bands (Peterson et al., 2004).

It has a 2–10 keV observed-frame flux of $F_{2-10\ \mathrm{keV}} \sim 4 - 9 \times 10^{-11}$ erg cm^{-2} s^{-1}, which corresponds to a luminosity of $L_{2-10\ \mathrm{keV}} \sim 1.5 \times 10^{43}$ ergs^{-1} (Reeves et al., 2004). Its bolometric luminosity is $L_{\mathrm{Bol}} = 2.57 \times 10^{44}$ ergs^{-1} (Woo and Urry, 2002), which is about 6% of Eddington luminosity (Brenneman et al., 2011).

It was first detected in X-rays by the Ariel-V all sky survey (McHardy et al., 1981) and subsequently in the high Galactic latitude survey conducted by HEAO-1 (Piccinotti et al., 1982). Since these early X-ray detections, there have been many observations of NGC 3783 in the X-ray band. A ROSAT observation of NGC 3783 showed evidence for a ionized absorber in the soft X-ray spectrum (Turner et al., 1993), which was confirmed during ASCA observations (George et al., 1998). Subsequent high-resolution grating observations of NGC 3783 with *Chandra* have revealed the soft X-ray absorber with unprecedented accuracy and resolution: strong absorption lines were found, due to N, O, Ne, Mg, Al, Si, S and Fe at different ionization states with velocities of ~ 600 km s^{-1} (Kaspi et al. (2000), Kaspi et al. (2001)). Analyzing XMM-*Newton* observation of 2001, Reeves et al. (2004) identified several features: a strong Fe Kα at 6.4 keV, an emission line at $\sim$7 keV due to a blend of Fe Kβ and H-like Fe, and absorption at $\sim$6.6 keV due to highly ionized Fe, plus an absorption edge at $\sim$7.1 keV. During a Swift monitoring program to track the hardness variability in type 1 AGN, NGC 3783 showed a heavy X-ray absorption produced by an obscuring outflow. As a result, new absorption lines from Fe XXV and Fe XXVI appeared in the spectrum. From their analysis, Mehdipour et al. (2017) found for the outflow a column density of a few 10^{23} cm^{-2} and a velocity of few 1000 km s^{-1}. It should be a clumpy, inhomogeneous medium consistent with clouds at the base of a radiatively-driven disk wind located the outer broad line

region of the AGN.

4.1 Observations and data reduction

There are a total of 7 observations for this source in the XMM-*Newton* Science Archive, but two of them (OBS ID 0112210401 and OBS ID 0112210601) were excluded from our analysis because of their short duration ($\sim$ 4 ks). The observations we used are listed in Tab. 4.1.

Revolution	**Observation ID**	**Duration** (s)	**Mean flux 4.5 - 12 keV** (10^{-11} erg s^{-1} cm^{-2})	**Start date** D/M/Y
193	0112210101	40412	3.673	28/12/2000
371	0112210201	137818	2.854	17/12/2001
372	0112210501	137815	3.499	19/12/2001
3115	0780860901	115001	*	11/12/2016
3120	0780861001	57000	*	21/12/2016

Table 4.1: All XMM-*Newton* observations we used of NGC 3783, from the 3XMM-DR7 catalogue. Informations for the fields marked with * were not available on the catalogue, as the corresponding observations were carried out after the last date considered in it.

We considered only the data from the pn because it is the instrument with the highest sensitivity (see Sect. 3 and Fig. 3.3), so the most suitable for our analysis. We obtained the calibrated fits files from the Observation Data Files (ODF) using the SAS task `EPPROC`. After using this task on data of revolution 371 we obtained two distinct observation sets, the first one (from now on identified as 371a) with $\sim$55 ks of exposure, the second one (371b) with $\sim$75 ks of exposure, and the two are separated by about 7 ks.

XMM-*Newton* data can often be contaminated by periods of high background flux, due to interactions of soft protons with the detectors. These energetic solar protons, trapped by the fields lines of Earth magnetosphere, can cause spurious peaks even a hundred times higher than the mean value in the light curves. The standard procedure to remove these artificial events is to extract a light curve at energies higher than 10 keV, where the effective area of the instrument drops and only non-focused events remain. The flux peaks are eliminated using a threshold on the count rate or selecting and removing the time intervals in which they appear.

Moreover, bright X-ray sources data can be affected by pile-up. This issue is due to the possibility that two or more photons impact on the same CCD pixel in a time shorter than the instrumental read-out time. In such cases they are identified as a single event with an energy equal to the sum of the two or more matching photons. Pile-up shall cause an artificial defor-

mation in the spectrum, in particular a spectral hardening because of the simultaneous increase of counts in the high-energy band and the decrease of counts in the lower ones. To check whether this effect is present in our data, we used the SAS task `EPATPLOT`. None of the observations showed significant indications of pile-up for NGC 3783.

The source spectra were extracted from circular regions with a radius of 45 arcsec containing $\sim$ 85% of the source counts (see Fig. 3.1) for on-axis positions, while background ones were collected from adjacent source-free regions, with radius of 65 arcsec, as shown in Fig. 4.1. Backgound-subtracted light-curves and spectra were then extracted, few examples are shown in Fig. 4.1.

4.2 Residual Maps

We then produced the residual maps, following the procedure described in Sect. 2.1. The continuum was first fit in two energy bands: 4.0-5.0 keV and 7.5-10.0 keV. The choice of the latter is due to an absorption feature in Observations 3115 and 3120, analyzed in Mehdipour et al. (2017). It is a broadened absorption extending from $\sim$6.5 keV to $\sim$7.5 keV, so we decided to avoid this interval to not contaminate the continuum fitting. Although this feature was not observed in previous observations, we used the same bands for all datasets.

Applicability For each observation we measured the count rate per keV (in Tab.4.2) in the whole 4.0-10.0 keV band and, in particular, in the 7.5-10.0 keV interval. Even using the smallest possible energy bins (ΔE=100 eV) and a time resolution as short as 2.5 ks, we are able to satisfy the condition of having at least 20 counts per pixel (see Tab.4.3).

Revolution	$<$**cts s^{-1}** keV^{-1} $>$	
	4.0 -10.0 keV	7.5 - 10.0 keV
193	0.5	0.2
371a	0.4	0.2
371b	0.4	0.2
372	0.5	0.2
3115	0.2	0.1
3120	0.3	0.1

Table 4.2: Mean value of counts per energy and time units in 4.0 - 10.0 keV and 7.5 - 10.0 keV energy bands for all NGC 3783 observations considered.

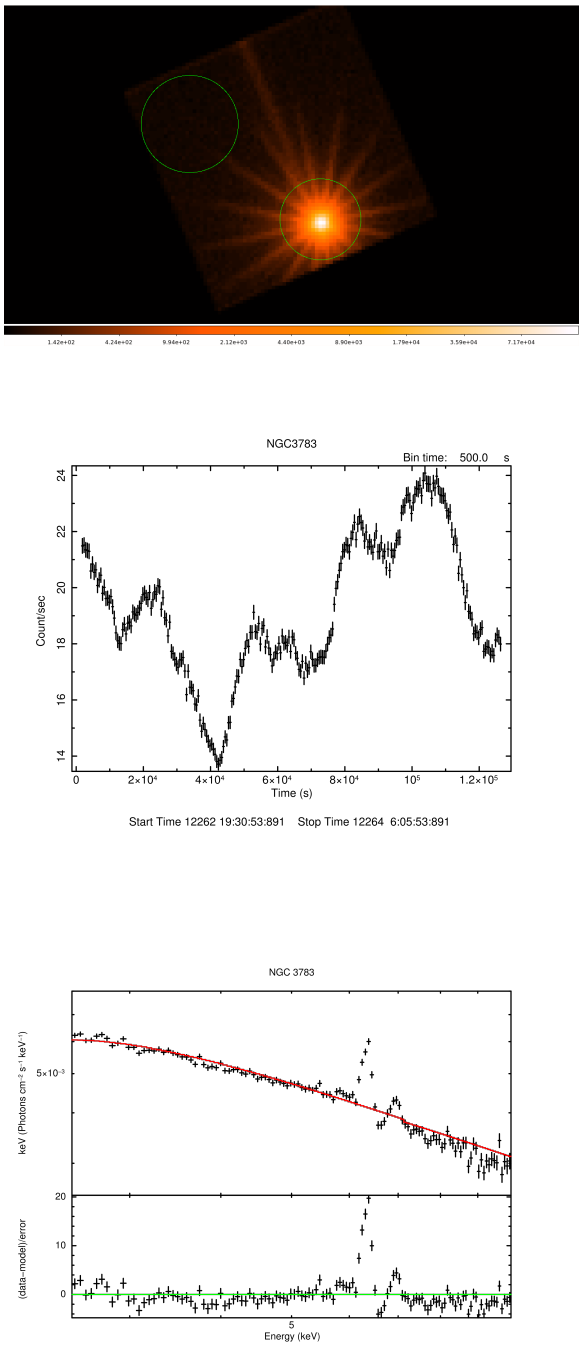

Figure 4.1: Upper panel: image of observation 372 of NGC 3783, with the extraction regions for the source and the background (in green). **Middle panel**: the light curve in the 0.3-10.0 keV energy range. Every time bin has a 500s-length. The source shows high variability, in particularly the count-rate vary of almost a factor 2 in few tens of ks, underlining the necessity of a time-resolved analysis. **Lower panel**: the 3-10 keV spectrum of the whole observation, fitted with a power law and the relative $\Delta\chi$. There is an evident Fe Kα and a second line at higher energy, probably a Fe Kβ or a Kα from ionized iron. From the presence of residuals below $\sim$5 keV and above $\sim$7 keV, it is clear that a good characterization of this source needs a more complex modeling.

Revolution	Counts per pixel	
	4.0 - 10.0 keV	7.5 - 10.0 keV
193	125	54
371a	94	43
371b	100	44
372	125	55
3115	63	29
3120	78	35

Table 4.3: Estimated values of counts per pixel in energy bands 4.0 - 10.0 keV and 7.5 - 10.0 keV, using a time resolution of 2.5 ks and an energy resolution of 0.1 keV for all NGC 3783 observations considered in this work.

4.2.1 Observation 3120

Among all the residual maps of NGC 3783, we found that obtained during observation 3120 to be particularly interesting, and so we decided to go for a deeper analysis using directly the X-ray spectra. As shown in Fig. 4.3 (lower-right panel) and 4.4 the principal emission component at ∼6.3 keV seems to vary nearly periodically, showing periods of higher intensity spaced with lower emission periods. We acknowledge four peaks, and four minima, and identify them as *high state* and *low state*, respectively. It is to be noted that we are only looking at the residual maps when stating this difference, i.e. we are not considering the actual count rate from a light curve to define the two "states".

The total observation is composed of 23 spectra, each of 2.5 ks duration. By looking at the map and counting the "high" and "low" single spectra, we decided the temporal cuts to apply to divide the total observation in the two states. We extracted spectra of these durations from the filtered observation file, adopting the same regions used in Sect. 4.1 and shown in Fig. 4.1. The spectra, their state and their duration are listed in Tab. 4.4.

We studied together the spectra in the same state, under the assumption that they share the same spectral shape, eventually with different flux for the continuum. This assumption is actually strong and not completely verified a priori, but it is good enough if we are just trying to identify the main differences between high and low states, as we actually do.

First we analyzed the high state. We started using a simple power law, as shown in Fig. 4.5. The spectral fit is not good, as expected given the premises above. However, we remind here that the purpose of this analysis consists in verifying whether the structures emerging from the residual map are real and at which level. From a visual inspection we see a prominent

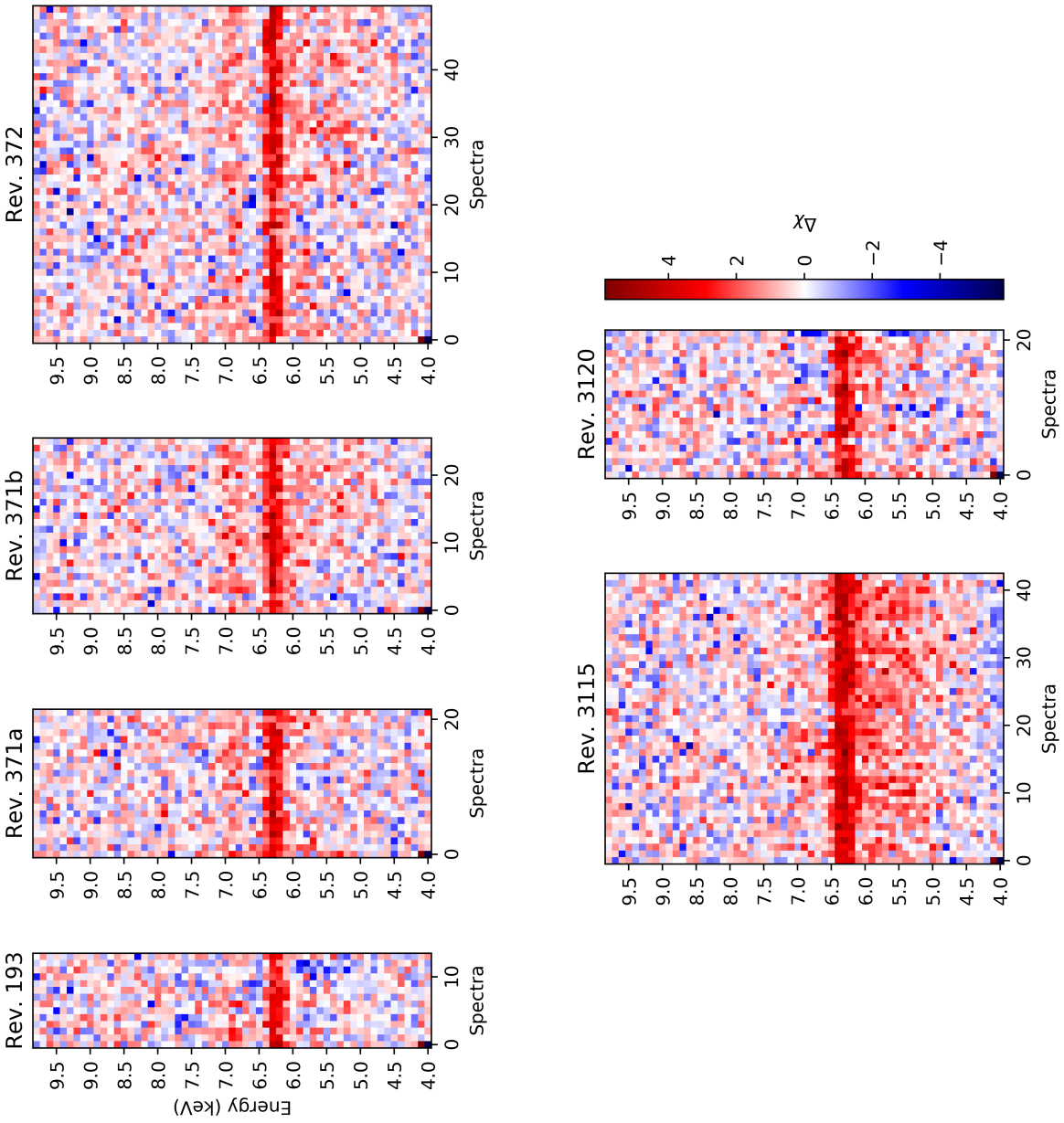

Figure 4.2: Residual maps of all NGC 3783 observations considered in this work, in chronological order.

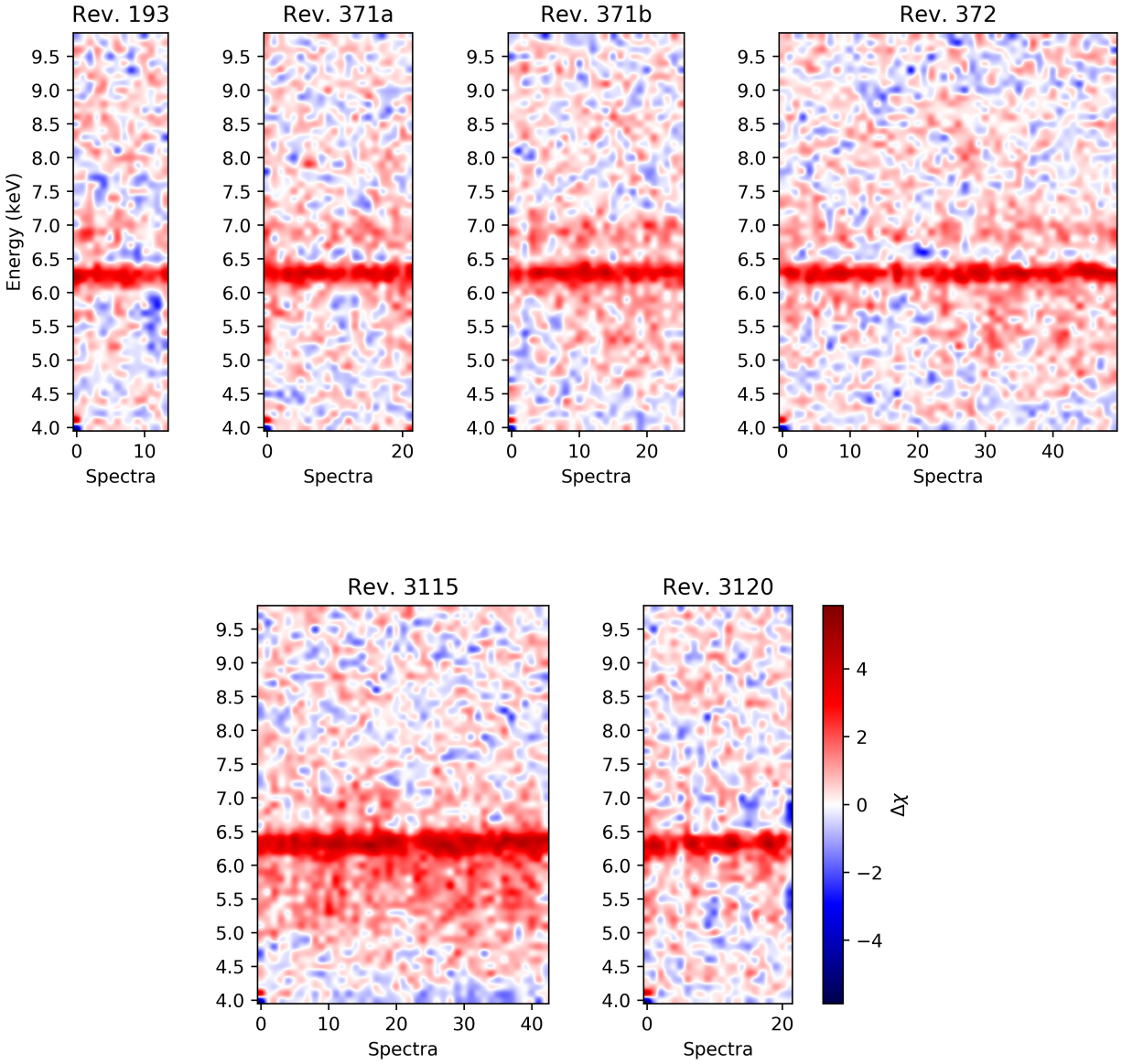

Figure 4.3: Smoothed residual maps of all NGC 3783 observations considered in this work, in chronological order.

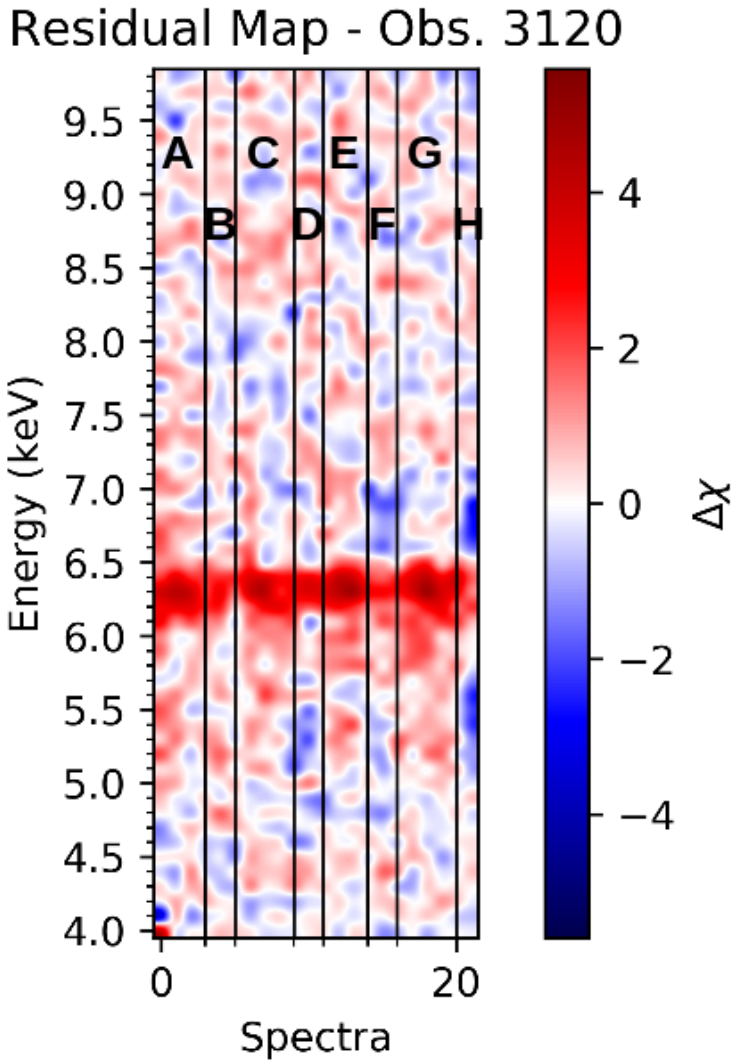

Figure 4.4: The smoothed residual map of observation 3120 of NGC 3783. The vertical black lines are the boundaries of the different states of the source, in which we divided the observation, as listed in Tab. 4.4.

Spectrum	State	Spectral interval	Duration (ks)
A	HIGH	0-2	7.5
B	LOW	3-4	5.0
C	HIGH	5-8	10.0
D	LOW	9-10	5.0
E	HIGH	11-13	7.5
F	LOW	14-15	5.0
G	HIGH	16-19	10.0
H	LOW	20-22	7.5

Table 4.4: List of spectra extracted from the Observation 3120 of NGC 3783. The numbers in the third column (spectral intervals) represent the first and last time bins included in each spectrum, respectively. This division is based on the visual inspection of the residual map, shown in Fig. 4.4.

peak at E$\simeq$ 6.4 keV, most likely being the neutral Fe Kα line. At energies red-ward of the line, there is a broad excess extended to about 3.5 keV, where there is a change in the trend, shown by the negative $\Delta\chi$. This curvature can be due to an absorption, so we add the component `phabs` to our model.

Analyzing the $\Delta\chi$ in Fig. 4.6 we see that, after adding the absorption component, the data seem to be more evenly distributed around the model and the excess at energies below the Fe Kα line is significantly reduced.

This second model (`phabs` and `powerlaw`) is the same we used when producing the residual maps, so we can make a direct comparison between what emerges from the spectral analysis and what our residual maps show.

In Fig. 4.7 we used arrows to pinpoint some interesting features, that we see both in the residual map and in the $\Delta\chi$ distribution. The magenta arrow points to the Fe Kα peaks in the map: all the spectra show such line with a similar profile and intensity.

Going redward we see an excess, most likely a broadened component of the line. All spectra show it at $\sim$ 5.9 keV and above, but at lower energies there are some differences: for example, the blue arrow shows the extended excess of spectrum G and the green arrow points to the absorption at $\sim$ 4.8 keV in spectrum E. Moving to higher energies we see significant scatter for all spectra, but spectrum G seems to be almost constantly below the model, as shown by the red arrow.

Moving to the low state we repeat the same procedure: first we modeled the spectra with a simple power law, as shown in Fig. 4.8, then we added

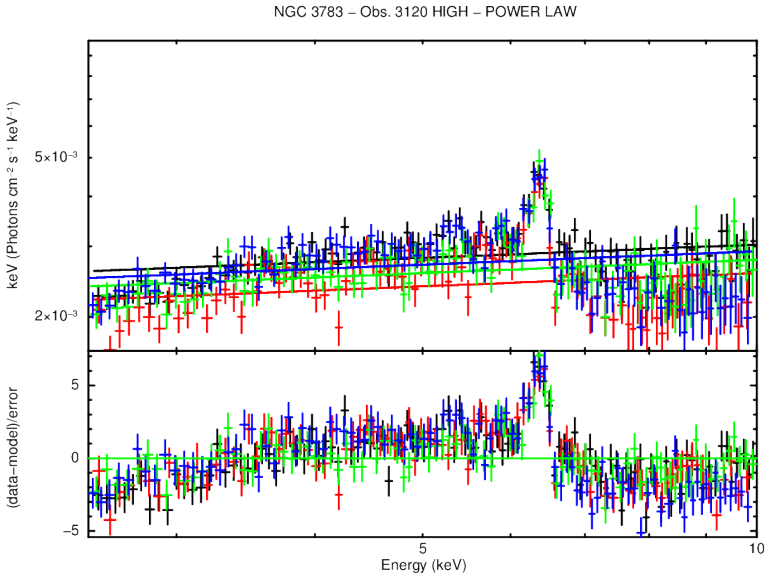

Figure 4.5: The four spectra of the high state modeled with a power law, in the upper panel, and their $\Delta\chi$ (i.e., data−model in units of σ), in the lower panel, in the energy band 2.5-10.0 keV. Spectrum A is in black, C in red, E in green and G in blue.

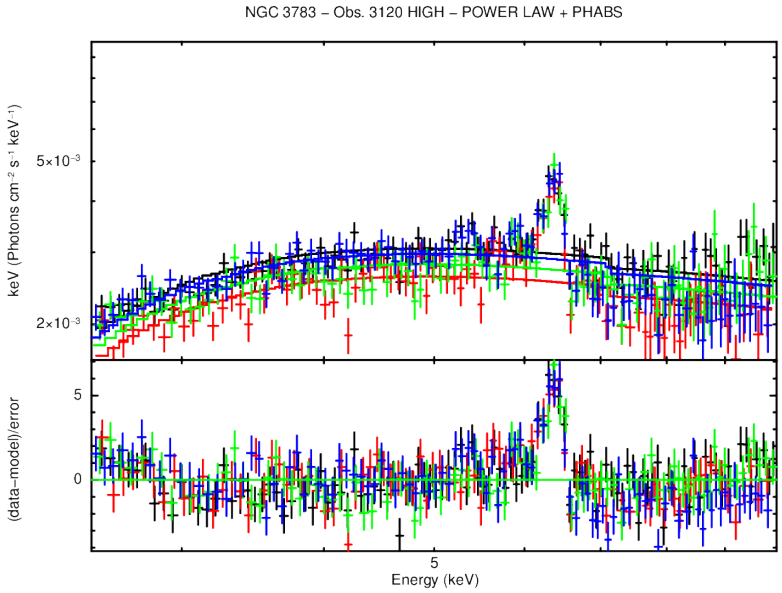

Figure 4.6: The four spectra of the high state modeled with a power law and cold absorption, in the upper panel, and their $\Delta\chi$, in the lower panel, in the energy band 2.5-10.0 keV. Spectrum A is in black, C in red, E in green and G in blue.

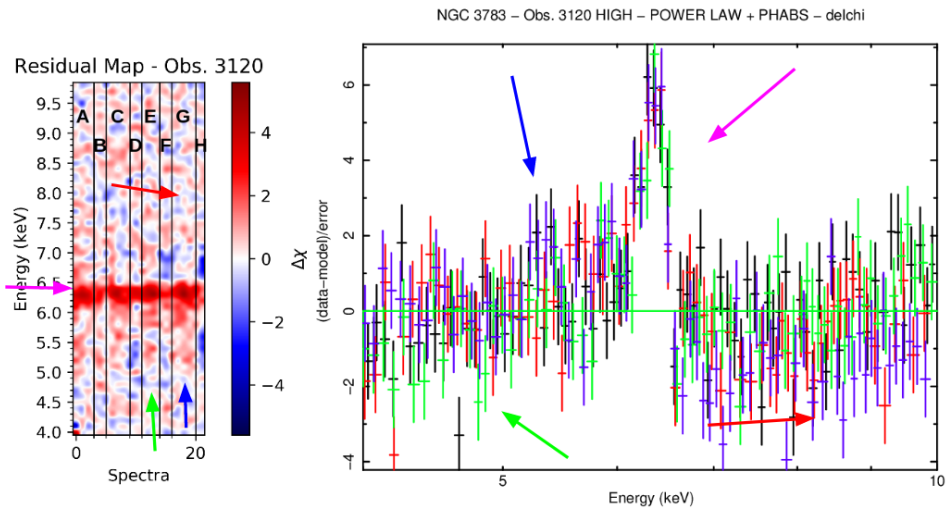

Figure 4.7: On the left the residual map of the whole observation, on the right the distribution of $\Delta\chi$ obtained adopting a power law and cold absorption model for the four high-state spectra of Observation 3120 of NGC 3783. Both are in the energy band 4-10 keV.

a cold absorption to reproduce the model used to make the maps, shown in Fig. 4.9.

We can again directly compare our spectral data in the band 4.0-10.0 keV to the map. In the low state the $\Delta\chi$ appear to be even more complex than in the high state. For example, the yellow arrow in Fig. 4.10 points to an absorption at an energy just below the Fe Kα in spectrum D, while the whole spectrum H seems to be in disagreement with the model, both at low and high energies, as indicated by the blue arrow. We see a complex distribution and a large scatter: this may be due to an augmented complexity in the model and/or to the strong variability experienced during this observation at this time. In Fig. 4.11 we see the light-curve of this observation with 500 s time bins, and towards the end the source appears to vary. Nevertheless, the spectra clearly confirm the lower intensity of the 6.4 keV emission line during the low state.

The high states are spaced out by fairly regular time intervals of $\sim$ 5-10 ks. Using equation 1.10 from Bardeen et al. (1972) for the computation of the orbital period at a fixed distance from the SMBH, considering a black hole mass of $\sim 3\times10^7 M_\odot$ (Peterson et al., 2004), we find that this emissivity could be originated in a range of $\sim$9-30 r_g, following the hot co-rotating flare model in Iwasawa et al. (2004).

It is clear, however, that the spectra we extracted from this observation are too different from each other to allow us a simultaneous modeling. In order to better quantify and the interpret the origin of measured Fe K

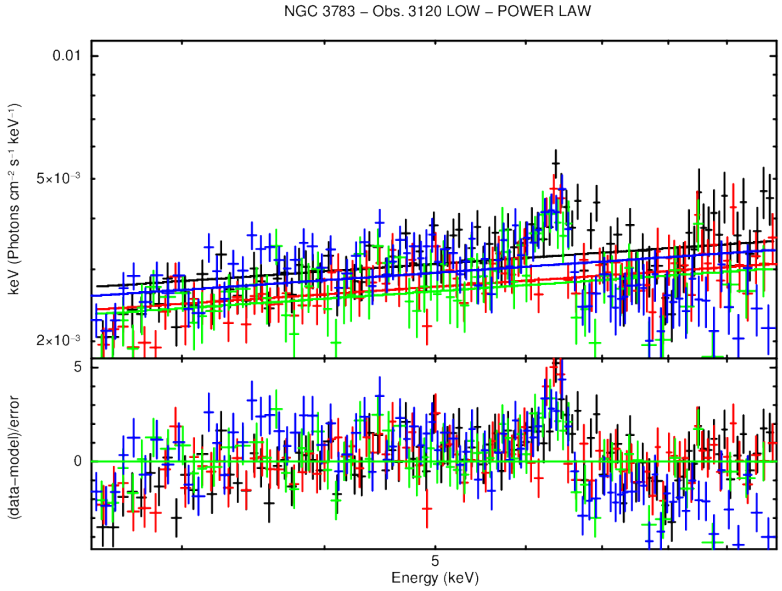

Figure 4.8: The four spectra of the low state modeled with a power law, in the upper panel, and their $\Delta\chi$, in the lower panel, in energy band 2.5-10.0 keV. Spectrum B is in black, D in red, F in green and H in blue.

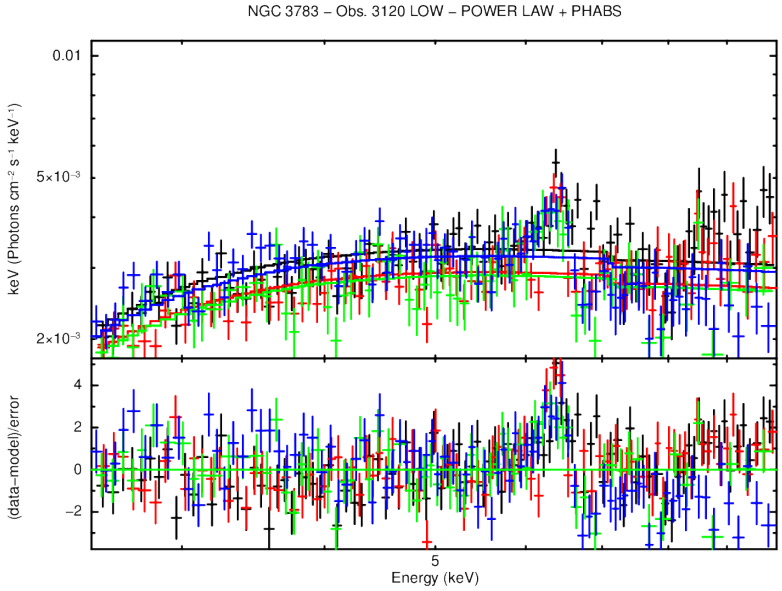

Figure 4.9: The four spectra related to the low state modeled with a power law and a cold absorption, in the upper panel, and their $\Delta\chi$, in the lower panel, in the energy band 2.5-10.0 keV. Spectrum B is in black, D in red, F in green and H in blue.

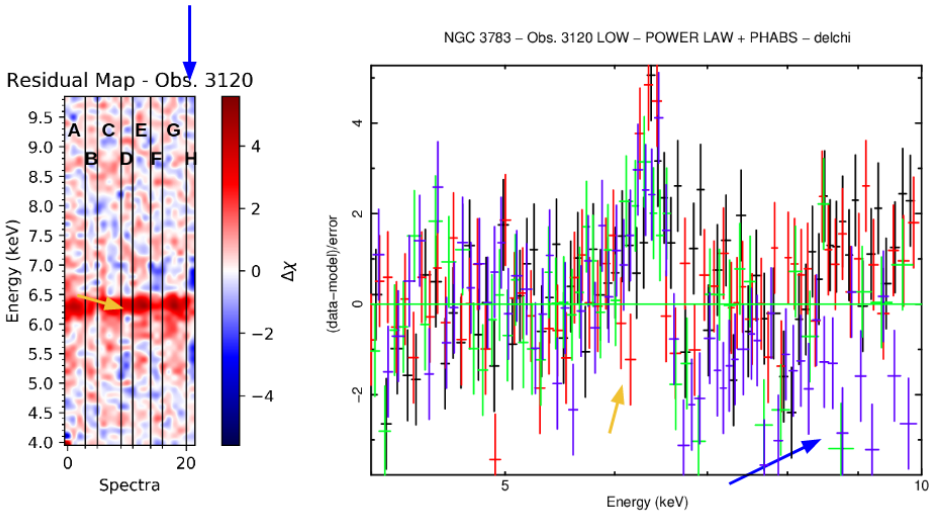

Figure 4.10: In the left panel the distribution of the $\Delta\chi$ of a power law and cold absorption model for the four low-state spectra of Observation 3120 of NGC 3783; on the right panel the residual map of the whole observation. Both are in energy band 4-10 keV.

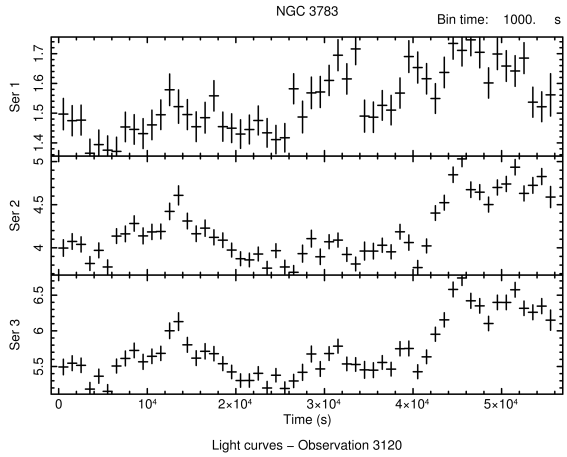

Figure 4.11: The light curves of the observation 3120 of NGC 3783, in the energy bands 0.1-3.0 keV, 3.0-10 keV and 0.1-10 keV, from top to bottom. Every bin has 500s duration. We see a very rapid variability (with changes occurring on time scales of $\sim$ 1 ks), although not all very intense, with flux changes of few counts/s.

line intensity and profile variability, they would need to be analyzed separately and with more complex components. For instance `zxipcf`, a model for partial covering absorption by partially ionized material, to better fit the observed absorptions at low energies, and `diskline` to characterize the relativistic-broadened line possibly appearing in the high state.

Summarizing, the analysis presented in this chapter is to be meant as preliminary and sets the stage for further and more complex investigation.

Chapter 5

Mrk 509

Mrk 509 is a bright Seyfert 1 galaxy at redshift of 0.034. Its black-hole mass, $M = 1.4 \pm 0.1 \times 10^8$ $M_\odot$, has been determined using the reverberation mapping method (Peterson et al., 2004). Mrk 509 has been one of the first AGN to be studied, thanks to its brightness, with a flux between 2 keV and 10 keV of $F_{2-10\ \mathrm{keV}} = 2 - 5\ \times 10^{-11}$ erg cm^{-2}s^{-1} (Kaastra et al., 2011).

Its bolometric luminosity is $L_{\mathrm{Bol}} = 1.07 \times 10^{45}$ ergs^{-1} (Woo and Urry, 2002) and its 2-10 keV luminosity is $L_X = 3 \times 10^{44}$ ergs^{-1} for energies between 2 and 10 keV (Pounds et al., 2001). The accretion rate $\dot{M}$ has a range between 20% and 30% of the Eddington rate (Petrucci et al., 2013) during the XMM-*Newton* campaign presented in Kaastra et al. (2011).

The first detection in the 2-10 keV band was made with Ariel V (Cooke et al., 1978). The soft-excess was first identified in this object thanks to HEAO1-A2 (Singh et al., 1985); the iron line was detected for the first time in 1987 with EXOSAT (Morini et al., 1987), and the reflection component was initially revealed by Ginga (Pounds et al., 1994). EPIC data from XMM-*Newton* observations (in 2000, 2001, 2005, and 2006) show evidence for a complex Fe K emission line, with a narrow and a neutral component possibly produced far from the source, plus a broad and variable component possibly originating in the accretion disk (Pounds et al. (2001); Page et al. (2003); Ponti et al. (2010); Ponti et al. (2013)). Using XMM-*Newton* observations of Mrk 509, Cappi et al. (2009) detected the presence of lines, at ∼8–8.5 keV and ∼9.7 keV, consistent with being produced by Fe Kα and Kβ shell absorptions associated with mildly relativistic and variable outflow (Boissay et al., 2014).

5.1 Observations and data reduction

Mrk 509 was observed with XMM-*Newton* a total of 17 times. Two of these observations were excluded in our analysis because of their too short duration (OBS ID 0130720401 of ∼8 ks and OBS ID 0306090101 of ∼4 ks).

The observations we used are listed in Tab. 5.1.

Revolution	**Observation ID**	**Duration** (s)	**Mean flux 4.5 - 12 keV** (10^{-11} erg s^{-1} cm^{-2})	**Start date** D/M/Y
161	0130720101	31636	2.329	25/10/2000
250	0130720201	44407	2.907	20/04/2001
1073	0306090201	85914	2.654	18/10/2005
1074	0306090301	47082	2.675	20/10/2005
1168	0306090401	69952	3.170	25/04/2006
1804	0601390201	60915	3.229	15/10/2009
1806	0601390301	63815	2.835	19/10/2009
1808	0601390401	60917	3.49	23/10/2009
1811	0601390501	60919	2.835	29/10/2009
1813	0601390601	62814	3.224	02/11/2009
1815	0601390701	63120	3.737	06/11/2009
1817	0601390801	60918	3.496	10/11/2009
1819	0601390901	60915	3.75	14/11/2009
1821	0601391001	65517	3.342	18/11/2009
1822	0601391101	62820	3.675	20/11/2009

Table 5.1: XMM-*Newton* observations of Mrk 509, from 3XMM-DR7.

We reduced the data using the same procedure used in Sect. 4.1. We extracted only pn data with `EPPROC` and filtered them from soft protons. We checked for pile-up with `EPATPLOT`: it was absent in all observations. We extracted the source spectra from 45 arcsec radius circular regions and background spectra from nearby regions free of contaminating sources. Background-subtracted light-curves and spectra were then extracted (see Fig. 5.1 for some examples of images, light-curves and spectra obtained). Then residual maps were obtained as detailed below.

5.2 Residual Maps

For this source we fit the continuum in the energy bands 4.0-5.0 keV and 7.0-10.0 keV.

Since the flux of this source is of the same order of that of NGC 3783, we did not repeat the applicability test to count the photons per pixel. We assumed to have the same results as the previous source and used the same resolutions: Δt=2.5 ks and ΔE=100 eV.

In the following we will focus on one of the observations, 1813, which has been chosen on the basis of its peculiar residual map, in which the Fe Kα is not visible in the first part of the observation but on only in the second one.

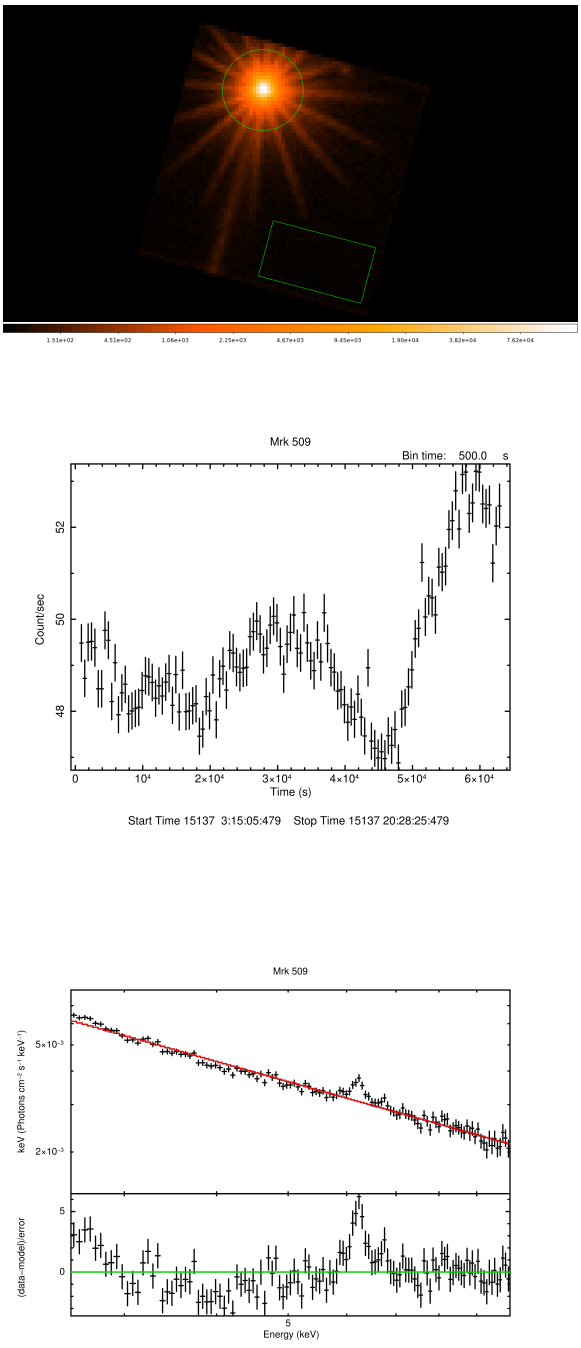

Figure 5.1: Upper panel: image of observation 1813 of Mrk 509, with the extraction regions for the source and the background (in green). **Middle panel**: the light curve in the 0.3-10.0 keV energy range, with 500s-length time bins. There is some variability (an increase from ∼47 to ∼53 counts/s in less than 10 ks), but this source is not as variable as the others we analyze in this work. **Lower panel**: the spectrum of the entire observation, fit only with a power law, and the $\Delta\chi$. The Fe Kα is clearly visible, and between ∼3.5 and 5 keV the $\Delta\chi$ show signs of an absorption that will need additional components to be better characterized.

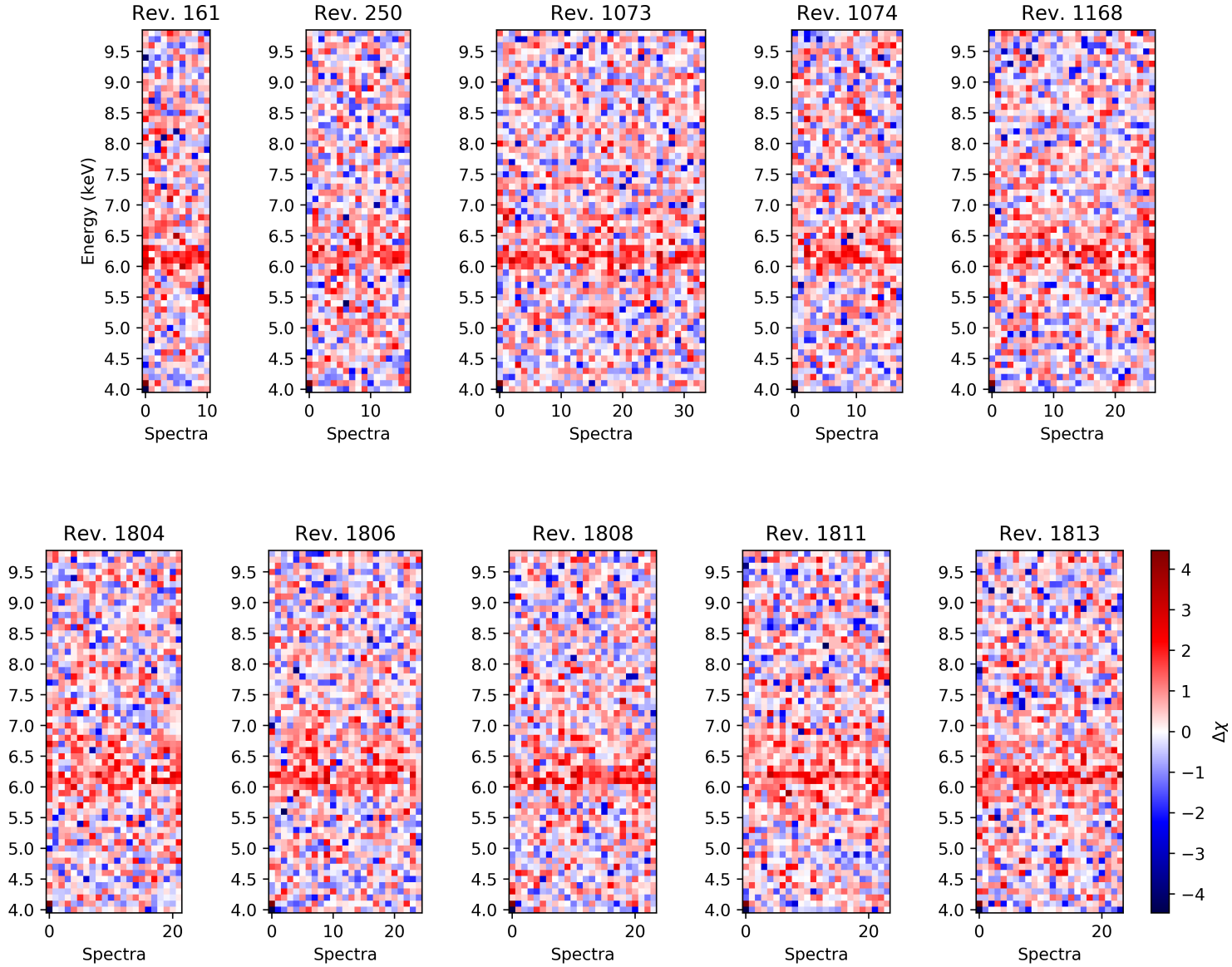

Figure 5.2: Residual maps of all Mrk 509 observations considered, in chronological order (part 1).

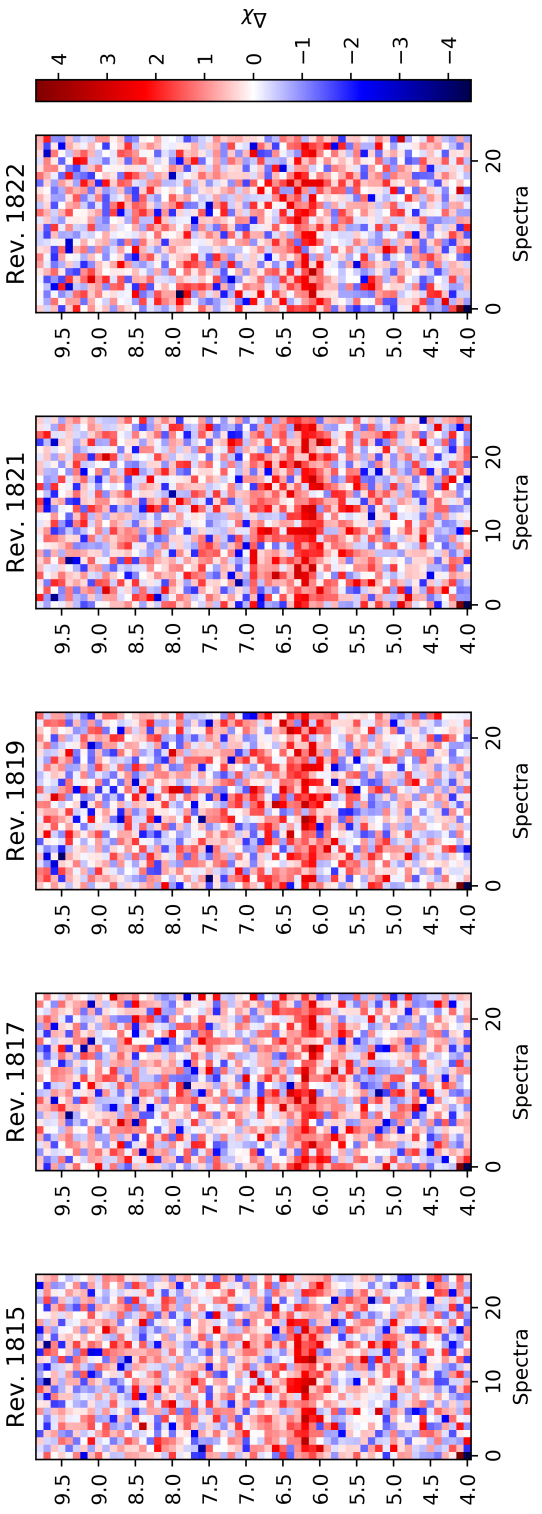

Figure 5.3: Residual maps of all Mrk 509 observations considered, in chronological order (part 2).

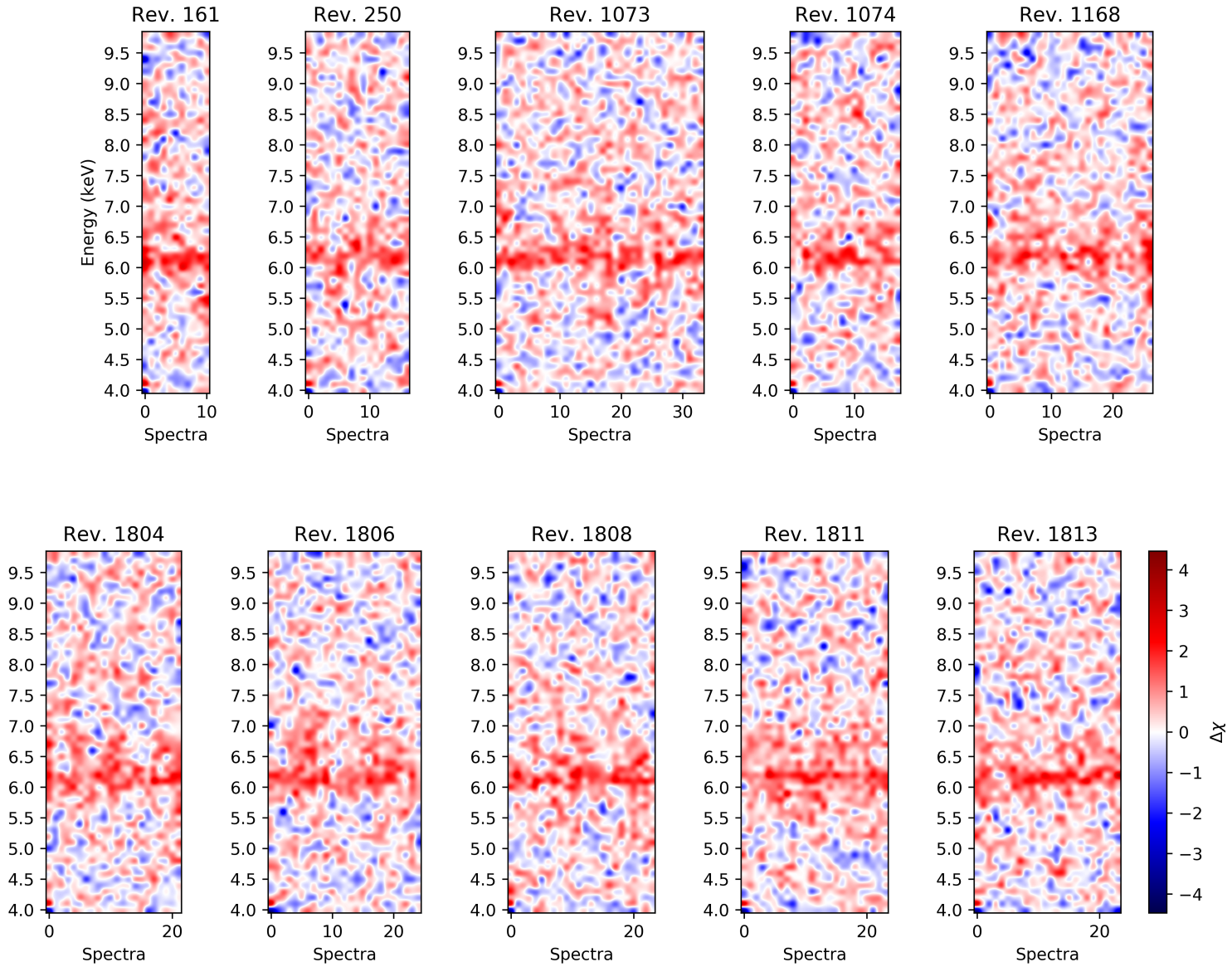

Figure 5.4: Smoothed residual maps of all Mrk 509 observations considered, in chronological order (part 1).

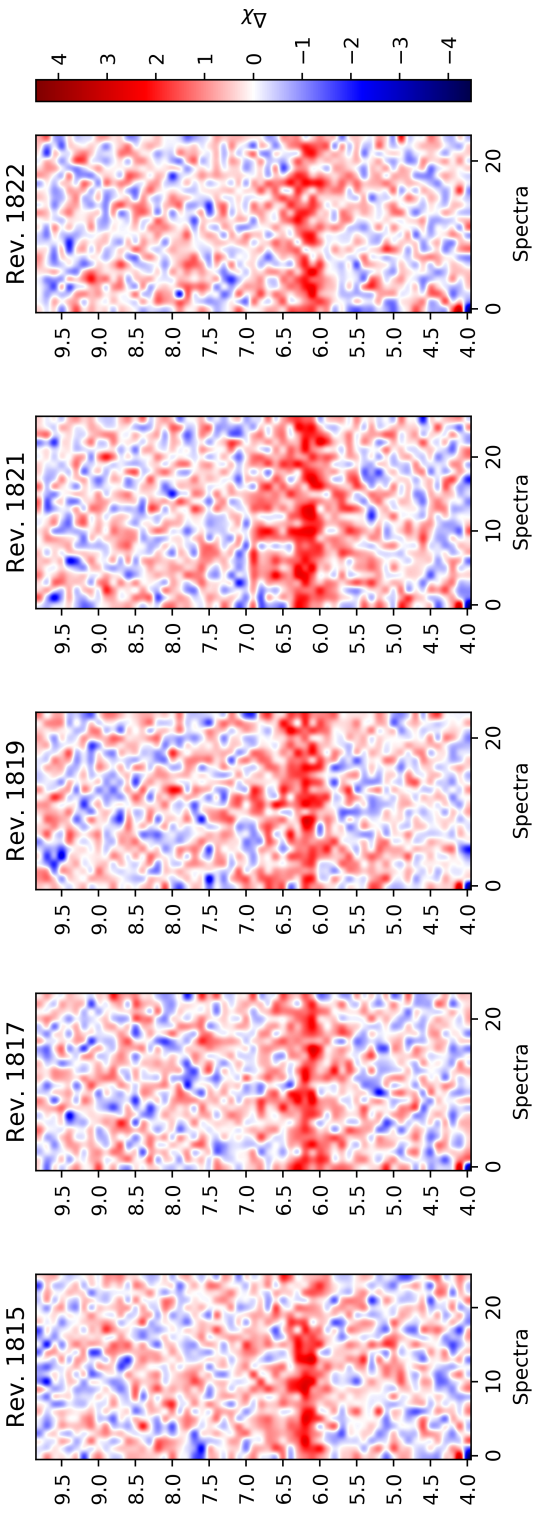

Figure 5.5: Smoothed residual maps of all Mrk 509 observations considered, in chronological order (part 2).

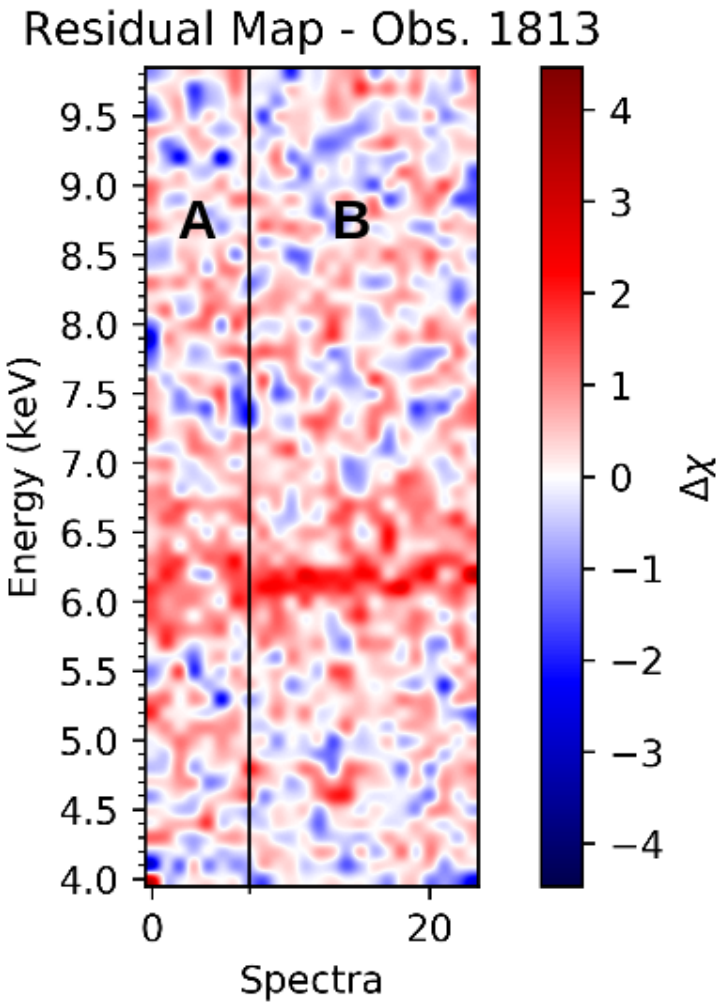

Figure 5.6: Smoothed residual map for the observation 1813 of Mrk 509. We identify two different regimes, separated here by the vertical black line: in the first part (A) there is not evidence for a narrow Fe Kα emission line, but there is a low-intensity excess extended from ∼5.7 to ∼7 keV. In the second part (B) a narrow feature emerges at ∼6.3 keV and the broader component is still present between ∼5.7 and ∼7 keV.

5.2.1 Observation 1813

Inspecting the residual map of observation 1813 we can spot two different behaviors in the $\sim 6.0 - 6.5$ keV band, as shown in Figure 5.6. The total observation is divided in 24 2.5 ks spectra. The first part (A) includes 8 spectra, for a duration of 20 ks, and in it we see a patchy excess, extending from ∼5.7 to ∼7.0 keV. In the rest of the observation (part B), that includes the last 16 spectra for a duration of 40 ks, a narrow feature arise at ∼6.3 keV, compatible with a Fe Kα.

We extracted the two spectra corresponding to the periods described above from the filtered observation file, from the same regions used in Sect. 5.1 and shown in Fig. 5.1, and analyzed them separately, following the same steps as in Sect. 4.2.1.

Starting from part A, we fit the spectrum with a simple power law, as shown in the upper panel of Fig. 5.7. The residuals appear scattered in the whole band: in particular we see an excess below ∼3 keV, at energies slightly lower then that of the Fe Kα and at $\sim$ 6.7 keV: it is already clear that a more complex model is needed. The lower-energy excess could be modeled with a `bbody` component: it represents a blackbody spectrum parametrized by its temperature expresses in keV and its normalization expressed in L_{39}/D_{10}^2, where L_{39} is the source luminosity in units of 10^{39} erg/s and D_{10} is the distance to the source in units of 10 kpc. For what concerns the ∼6 keV excess, it could be due to a red wing component of a cold iron line and/or to a possible smoothed absorption due to ionized matter, and it is clearly visible in Fig. 5.8. The narrower feature at ∼6.7 keV could be a Fe Kα from ionized material.

We then added the `phabs` component to replicate the model used to produce the residual maps but, as shown in the lower panel of Fig. 5.7, there is no difference from the previous model. In fact, the column density of the absorber is consistent with zero.

Applying the same procedure to spectrum B we find once again that the absorber is absent, as shown in Fig. 5.9. However, in this case the residuals show a prominent Fe Kα line at ∼6.4 keV (shown also in Fig. 5.10), absent in spectrum A. Below ∼3 keV there is an excess, as in spectrum A. Around ∼4 keV there are complex absorption features.

The reason of this sensible change in the spectrum is not clear, as stated for the analysis in Sect. 4.2.1 an accurate spectral analysis is necessary to unravel the phenomena causing this kind of variability.

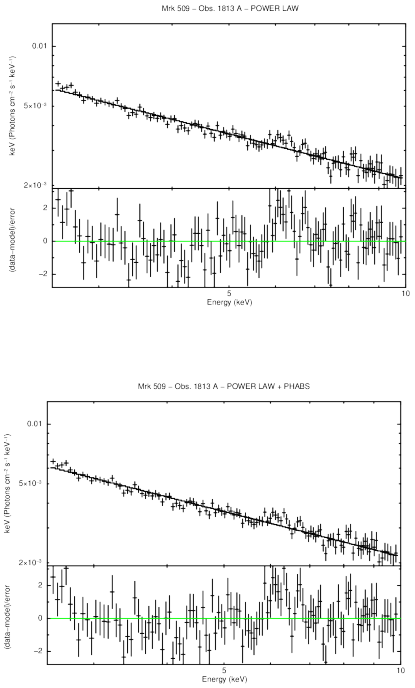

Figure 5.7: Spectrum A of the observation 1813 of Mrk 509. **Upper panel**: fit with the pure power law model. **Lower panel**: fit with power law and cold absorption. The models and the residual are exactly the same, meaning that the simple absorber we used has no effect on the modeling, as its column density is consistent with 0. Other components are obviously needed to fit the data. The residuals around 6.4 keV may indicate the presence of a very low-intensity Fe Kα line.

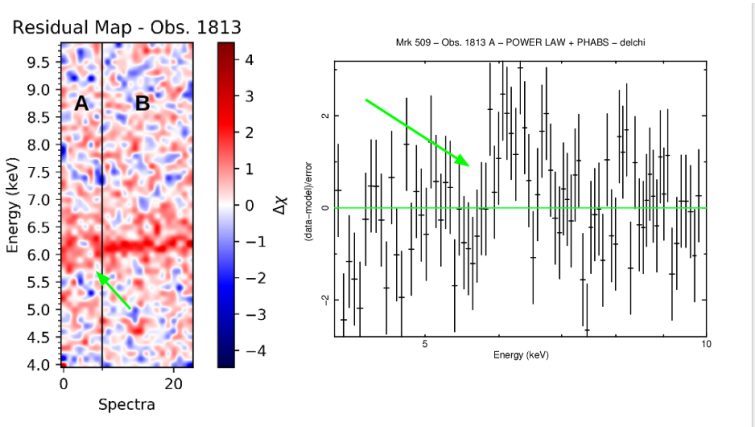

Figure 5.8: Direct comparison of the residual map and the $\Delta\chi$ of spectrum A. The green arrow points to the broadened component present in both.

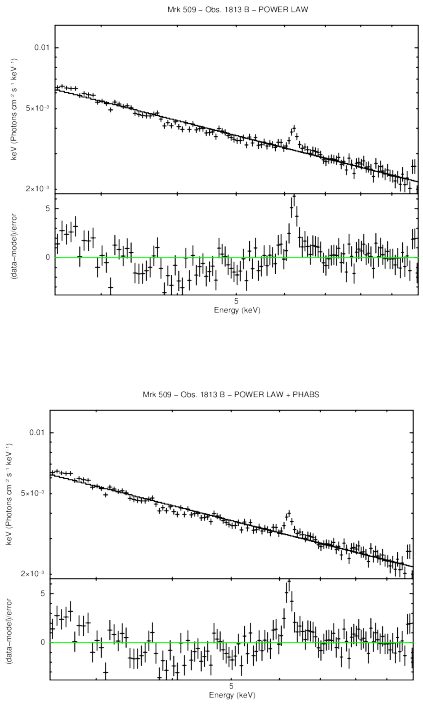

Figure 5.9: Spectrum B of the observation 1813 of Mrk 509. **Upper panel**: fit with a single power law model. **Lower panel**: fit with power law and cold absorption. As in spectrum A the cold absorption component has no effect. There is an evident Fe Kα line. Residuals show complex absorptions at energies around $\sim$4 keV.

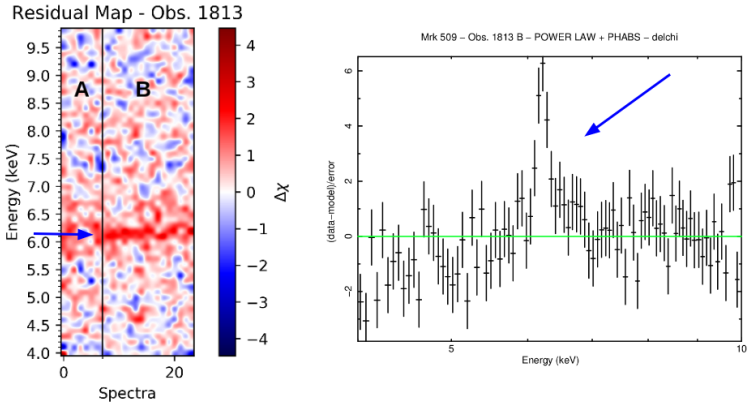

Figure 5.10: Direct comparison of the residual map and the $\Delta\chi$ of spectrum B. The blue arrow points to narrow Fe Kα line.

Chapter 6

IRAS 13224-3809

IRAS 13224-3809 is a Narrow Line Seyfert 1 (thereafter NLS1). NLS1 are AGN showing a strong anti-correlation between the strength of [O III] and Fe II lines in the optical spectra (Gallo, 2006), much softer X-ray spectra than Seyfert 1 with broader lines and typically remarkably rapid and giant amplitude variability (Boller, 1999). The model that best describes such emission predicts small mass black holes and high accretion rates, near to the Eddington limit, thought to be active galaxies in their earliest phase (Mathur, 2000).

IRAS 13224-3809 is at low redshift, $z = 0.0658$. Its central SMBH has a low mass, $M_{BH} \sim 10^6$ $M_\odot$ (Zhou and Wang (2005); Kaspi et al. (2000)). It has an X-ray flux of $F_{0.3-10\ keV} \sim 4 \times 10^{-12}$ erg cm^{-2} s^{-1} (Pinto et al., 2018) and is a very soft source, with a luminosity of $L_{0.1-2.4\ keV} \sim 3 \times 10^{44}$ erg s^{-1} (Boller et al., 1993). It is one of the most X-ray variable NLS1 galaxies known, showing large amplitude variability in all previously targeted observations: ROSAT (Boller et al., 1997); ASCA (Dewangan et al., 2002). IRAS 13224–3809 was first observed with XMM-*Newton* in 2002 for 64 ks (Boller et al. (2003); Gallo (2004); Ponti et al. (2010)). IRAS 13224–3809 in 2016 was the target of a very deep observing campaign with XMM-*Newton*, with observations totalling 1.5 Ms, as well as 500 ks simultaneously with NuSTAR. Results from this campaign so far include the discovery of flux-dependent ultrafast outflow (v/c∼0.24) (Parker et al., 2017). The UFO varies in response to the source continuum brightness (Pinto et al., 2018).

6.1 Observations and data reduction

This source was observed during a 1.5 Ms continuous campaign with XMM-*Newton*. There are a total of 12 observations of about 140 ks each, performed between 08/07/2016 and 09/08/2016 (Tab. 6.1). We decided to focus only on these consecutive observations, as we had already a long enough exposure, and ignore the previous older datasets, which consist of four ∼130 ks

observations in 2011 and one ∼64 ks observation in 2002.

Once again we followed the procedure described in Section 4.1. We reduced only pn data, extracted using the SAS task `EPPROC`, and filtered to remove the periods of intense soft protons flares. Using `EPATPLOT` we verified the absence of pile-up. To extract source spectra we used here smaller circular regions of 17" w.r.t the previous two sources; this radius includes ∼ 70% of the PSF (Fig. 3.1). This is because Chartas et al. (in preparation) have shown that this choice is preferred to reduce the background and increase the signal-to-noise ratio in this steep-spectrum source. In fact, using a more typical extraction region radius of 45" the background would start to dominate over the source flux at energies above ∼ 7.5 keV, thus producing unreliable results. The spectra shown in Fig. 6.1 (a and b) illustrate this problem. Examples of images and background-subtracted light-curves are shown in Fig. 6.2.

Revolution	**Observation ID**	**Duration** (s)	**Mean flux 4.5 - 12 keV** (10^{-13}erg s^{-1} cm^{-2})	**Start date** D/M/Y
3037	0780560101	141300	3.951	08/07/2016
3038	0780561301	141000	3.576	10/07/2016
3039	0780561401	138100	3.470	12/07/2016
3043	0780561501	140800	2.434	20/07/2016
3044	0780561601	140800	5.159	22/07/2016
3045	0780561701	140800	2.851	24/07/2016
3046	0792180101	141000	2.999	26/07/2016
3048	0792180201	140500	3.161	30/07/2016
3049	0792180301	140500	3.006	01/08/2016
3050	0792180401	140800	7.608	03/08/2016
3052	0792180501	138000	3.727	07/08/2016
3053	0792180601	136000	6.706	09/08/2016

Table 6.1: XMM-*Newton* observations of IRAS 13224-3809 of the 2016 1.5 Ms campaign. Data are from 3XMM-DR7.

6.2 Excess maps applicability

IRAS 13224-3809 was specifically added to the sample because it showed several interesting properties. The analysis done in Parker et al. (2017) points to the presence of a UFO absorption with an equivalent width of 0.26 keV at 8.6 keV, corresponding to a stationary velocity of the outflow of 0.236 c. Different results were obtained in the recent re-analysis by Chartas et al., where the UFO shows variability in both strength and energy. These phenomena should in principle appear on residual maps, which could help

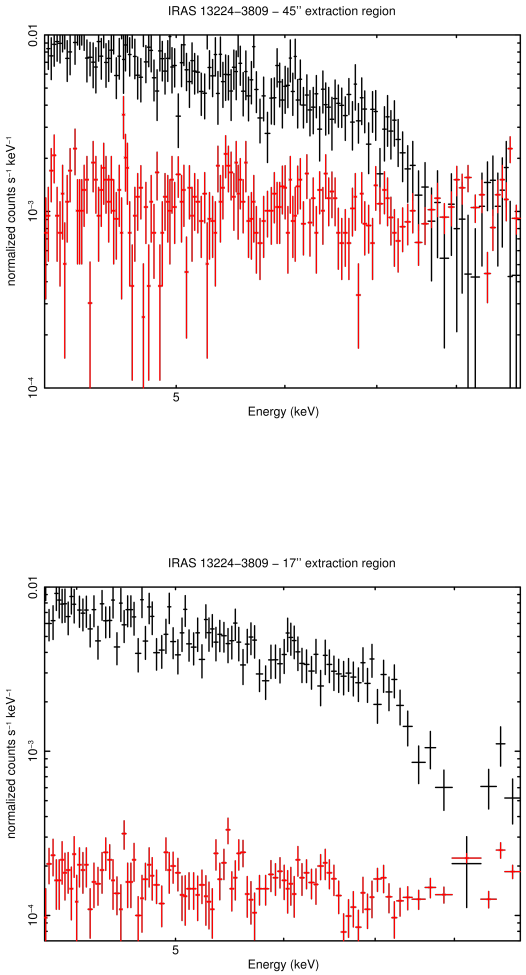

Figure 6.1: Spectra in the 4-9 keV energy range for of the observation 3048. In the upper panel the circular extraction region has a 45" radius: at energies above $\sim$ 7.5 keV the source flux (black points) is swamped by the background (red points). In the lower panel the extraction region is a 17" radius circle: the background has a sensibly lower flux than the source.

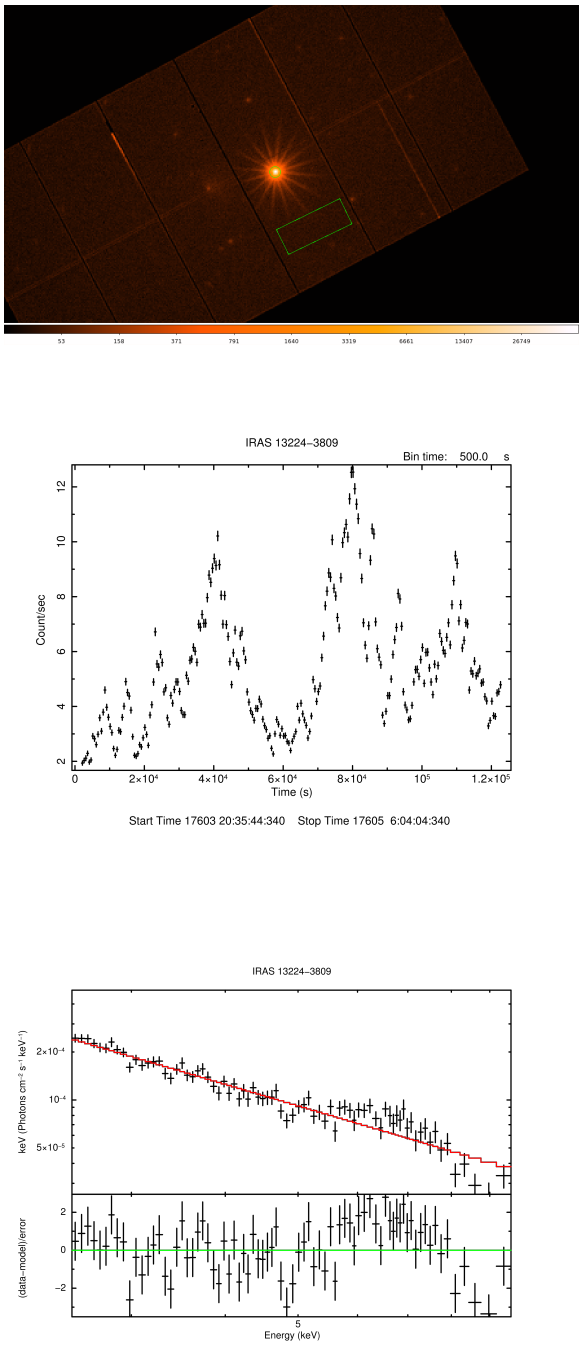

Figure 6.2: Upper panel: image of the observation 3050 of IRAS 13224-2809, with the extraction regions for the source and the background (in green). **Middle panel**: the light curve in the range 0.3-10.0 keV, with 500 s time bins. This source shows the highest variability in our sample, with changes in the count rate up to a factor 6 in less than 20 ks.**Lower panel**: the spectrum of the whole observation fitted with a power law, and the relative $\Delta\chi$. Seeing such a high variability, the study of the average spectrum of the observation is undoubtedly not sufficient to characterize the phenomena in act in this source, and a time resolved analysis in definitely needed.

to finally discern the best characterization for this source. Unfortunately, we were not able to apply this technique on IRAS 13224-3809 because of its low flux: as stated in Section 2.1.1, we need to have at least 20 counts in each pixel of the map to be able to apply a χ^2 minimization fitting.

Despite the low source flux, we checked if it would be feasible to produce the residual maps with a meaningful number of photons per pixel. For each observation we measured the mean value of counts per second in the energy band 4.0 - 9.0 keV and, in particular, in the higher energy range of 7.0 - 9.0 keV, where we expect to see the features produced by the UFO (Parker et al., 2017).

Revolution	10^{-3}<**cts** s^{-1} keV^{-1} >	
	4 - 9 keV	7 - 9 keV
3037	6	2
3038	7	2
3039	2	1
3043	4	1
3044	9	2
3045	5	1
3046	5	1
3048	6	1
3049	4	1
3050	13	4
3052	7	2
3053	12	3

Table 6.2: Mean value of counts per energy and time units in the bands 4.0 - 9.0 keV and 7.0 - 9.0 keV for 2016 observations of IRAS 13224-3809.

Table 6.2 shows that the lowest source flux value was registered for the observation 3039 and the highest for the observation 3050. To establish the applicability of the residual map technique also to IRAS 13224-3809, we used these two extreme pointings plus the observation 3048, which has an average value for what concerns its count rate. The three spectra corresponding to these three cases are reported in Fig. 6.3. We calculated the expected number of counts for different time resolutions (2.5 ks, 10 ks, 25 ks, 50 ks) and energy resolutions (100 eV, 200 eV, 300 eV), the results are listed in Table 6.3.

We find that, to reach the minimum of 20 counts per pixel in the high-energy band, even in the observation with the highest flux, it is necessary to use at least a time resolution of 25 ks and an energy resolution of 0.2 keV. With a central black hole of $M_{BH} \sim 10^6 M_\odot$ and a spin parameter $a = 0.99$ (Parker et al., 2017), the orbital period at $\sim 10\ r_g$ is as short as ~ 6000 s,

Energy band	Energy resolution eV	Time resolution 2.5 ks	10 ks	25 ks	50 ks
Observation 3039					
4.0 - 9.0 keV	100	0.6	2.2	4.5	11.3
	200	1.1	4.5	9.0	22.5
	300	1.7	6.8	13.5	33.8
7.0 - 9.0 keV	100	0.2	1.0	2.0	5.1
	200	0.5	2.0	4.1	10.3
	300	0.8	3.1	6.2	15.4
Observation 3048					
4.0 - 9.0 keV	100	1.4	5.7	11.4	28.5
	200	2.8	11.4	22.8	57.1
	300	4.3	17.1	34.2	85.6
7.0 - 9.0 keV	100	0.4	1.5	3.0	7.4
	200	0.7	3.0	6.0	14.9
	300	1.1	4.5	9.0	22.4
Observation 3050					
4.0 - 9.0 keV	100	3.2	13.1	26.2	65.5
	200	6.5	26.2	52.4	130.9
	300	9.8	39.3	78.5	196.4
7.0 - 9.0 keV	100	0.9	3.8	7.5	18.9
	200	1.8	7.5	15.1	37.7
	300	2.8	11.3	22.6	56.6

Table 6.3: Counts per pixel with different combinations of time and energy resolutions for observations 3039, 3048 and 3050 of IRAS 13224-3809.

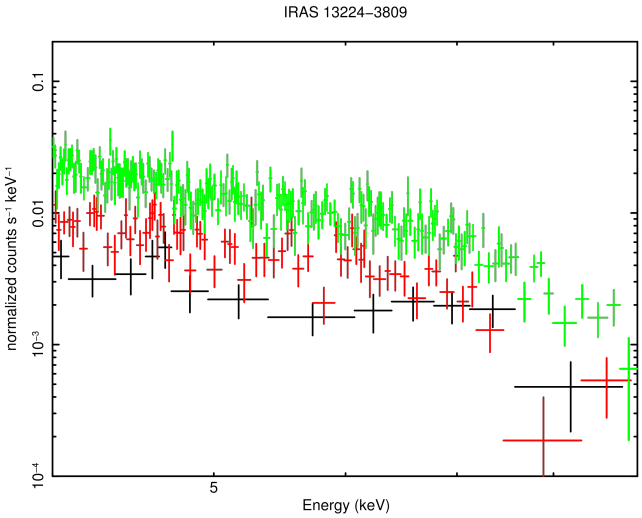

Figure 6.3: 4.0 - 9.0 keV spectra of observations 3039, 3048 and 3050 of IRAS 13224-3809, in black, red and green, respectively. These three datasets correspond with the lowest, average and highest statistics for this source.

and to oversample it we should integrate on even shorter times. Moreover, a 0.2 keV energy resolution cannot be used to properly analyze narrow lines, as the one found for UFO absorption in Parker et al. (2017).
We conclude that for sources as faint as IRAS 13224-3809, this technique is not suitable to study variability originated from the innermost regions, while it could be still used, of course, to analyze variations on longer time scales.

Chapter 7

Reliability of the residual map method

We obtained interesting results using the residual map technique for two out of our three sources (see chapters 4 and 5). In total we have 21 observations of various durations (from $\sim$ 31 ks to $\sim$ 138 ks) for the two sources, 6 for NGC 3783 and 15 for Mrk 509. On each of these observations we carried out a series of tests, trying to verify the reliability of the residual map method: in particular, we searched for systematics that may be due primarily to the model used for the fit of the continuum.

7.0.1 Excess/absorption "balance"

In principle, in the bands where we fit the continuum we expect to see the same number of pixels with positive and negative residuals, but actually we see a predominance of positive values in both energy intervals for both sources. The counts are listed in Tab. 7.1 for NGC 3783 and in Tab. 7.2 for Mrk 509.

In the low-energy band (4.0 - 5.0 keV for both sources) the positive pixel fraction spans from 0.49 to 0.55, with a median value of 0.52. It is to be noted that only in two observations (revolutions 1815 and 1819 of Mrk 509) there is a majority of negative pixels.

In the high-energy band (7.5 - 10.0 keV for NGC 3783 and 7.0 - 10.0 keV for Mrk 509) the discrepancy is larger. There is always a majority of positive pixels, with an average fraction of 0.57, spanning in a range from 0.55 to 0.60.

The same problem can be seen by analyzing the light curves of the residuals, as shown below.

	4.0 - 5.0 keV					7.5 - 10.0 keV				
Revolution	**Total pixels**	**Res** ≥ 0	%	**Res <0**	%	**tot pixel**	**Res** ≥ 0	%	**Res <0**	%
193	140	72	51	68	49	336	192	57	144	43
371a	220	113	51	107	49	528	292	56	236	44
371b	260	131	50	129	50	624	353	57	271	43
372	500	265	53	235	47	1200	676	56	524	44
3115	430	230	53	200	47	1032	599	58	433	42
3120	220	117	53	103	47	528	301	57	227	43

Table 7.1: Number of positive and negative pixels in the bands used for fitting the continuum (4.0-5.0 and 7.5-10.0 keV), with corresponding percentage considering all pixels included in the same band, for all residual maps of NGC 3783.

	4.0 - 5.0 keV					7.0 - 10.0 keV				
Revolution	**Total pixels**	**Res ≥ 0**	%	**Res <0**	%	**tot pixel**	**Res ≥ 0**	%	**Res <0**	%
161	110	57	52	53	48	319	192	60	127	40
250	170	86	51	84	49	493	284	58	209	42
1073	340	178	52	162	48	986	570	58	416	42
1074	180	95	53	85	47	522	289	55	233	45
1168	270	141	52	129	48	783	447	57	336	43
1804	220	118	54	102	46	638	363	57	275	43
1806	250	133	53	117	47	725	412	57	313	43
1808	240	129	54	111	46	696	396	57	300	43
1811	240	125	52	115	48	696	396	57	300	43
1813	240	131	55	109	45	696	387	56	309	44
1815	250	122	49	128	51	725	401	55	324	45
1817	240	128	53	112	47	696	406	58	290	42
1819	240	118	49	122	51	696	390	56	306	44
1821	260	139	53	121	47	754	413	55	341	45
1822	240	126	52	114	48	696	391	56	305	44

Table 7.2: Number of positive and negative pixels in the bands used for fitting the continuum (4.0-5.0 and 7.5-10.0 keV), with corresponding percentage considering all pixels included in the same band, for all residual maps of Mrk 509.

7.0.2 Residual light curves

The same lack of balance between positive and negative pixels is present when the analysis of the residual light-curves is carried out. To calculate them we sum up residuals in pixels included in the energy bands listed in Tab. 7.3. Every point of the light-curve represents the sum of residuals in a single spectrum in a fixed band.

Energy Range keV
4.0 - 5.4
5.4 - 6.1
6.1 - 6.5
6.5 - 6.8
6.8 - 7.2
7.2 - 8.0
8.0 - 10.0

Table 7.3: Energy bands used to calculate the light curves of the residuals.

In the lowest and highest energy bands we expect light-curves scattered around zero. In fact, in the same energy intervals we fit the continuum and, by its very definition, the best fit curve is the function that best represents the distribution of the data, that should therefore be randomly scattered above and below it. Instead, as already stated in the previous section, we typically see an excess, as shown in Fig. 7.1 for NGC 3783 and in Fig. 7.2 for Mrk 509. The light curves in the other bands could, in principle, be used as an indicator for variability of single features: for example, the 6.1-6.5 keV energy band is ideal for the Fe Kα line and the 5.4-6.1 keV energy band for the relativistic-broadened emission, while the 6.8-7.2 keV and 7.2-8.0 keV are the best ones to search for UFO absorptions.

The reason why in the 4-5 keV band we are closer to the 50-50 proportion that we expect to see between positive and negative pixels may be due to the fact that it is the one with more counts, hence more spectral bins to fit than at higher energy. Therefore, if there is an intrinsic difference in the spectral shape between the two bands, the low-energy trend would prevail.

It is possible that we are observing, in the hardest bands, the fact that the adopted model is oversimplified. A neutral reflection component may be present in the spectrum thus producing an increase the flux at energies above $\sim$7 keV. Since it is not accounted for in our simple modeling, it causes an excess with respect to the model.

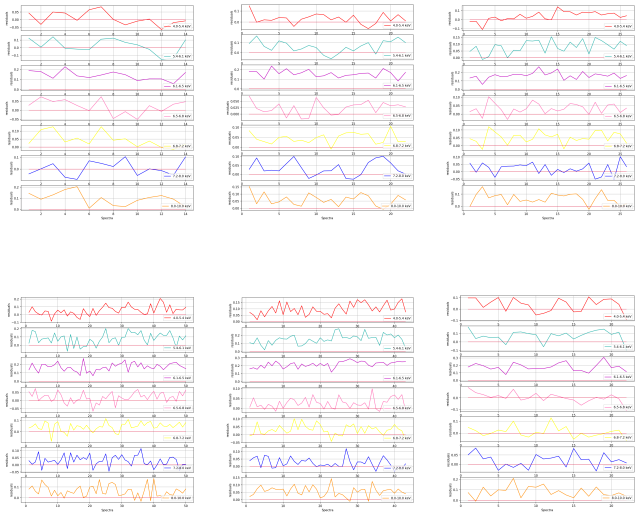

Figure 7.1: The light curves of the residuals for all observations used in the analysis of NGC 3783 and for all the energy bands listed in Tab. 7.3.

7.0.3 Photon index vs N_H

In the adopted simple model in each spectrum we leave both the photon index Γ of the `power law` component and the hydrogen column density N_H of the obscurer (that we parametrize with the `phabs` model in Xspec) free to vary to find the best possible fit. We verified whether there is a correlation between these two parameters.

For many spectra the N_H is consistent with zero, in particular this happens always for Mrk 509. Results are shown in Fig. 7.3 for NGC 3783. In NGC 3783 it varies from 0 to a maximum of $\sim 20 \times 10^{22}$ cm^{-2}. Γ values are in a range from $\sim$ 1.0 to $\sim$ 2.0, but most values span in the interval 1.6 - 2.0. Where N_H is not zero, there is a correlation with Γ due to their intrinsic degeneracy: the presence of an absorber causes a decrease of the flux at lower energies and so a change in the overall spectral shape.

7.0.4 Photon index vs line intensity

To verify whether the features that appear in the residual maps may have a strong dependence upon the continuum model, we searched for a correlation between the photon index of the power law and the intensity of the Fe Kα line.

At first we checked whether there is a correlation with the narrow line. As a measure of its intensity we summed up the residuals in pixels with

Figure 7.2: The light curves of the residuals for all observations we used in the analysis of Mrk 509, for all the energy bands listed in Tab. 7.3.

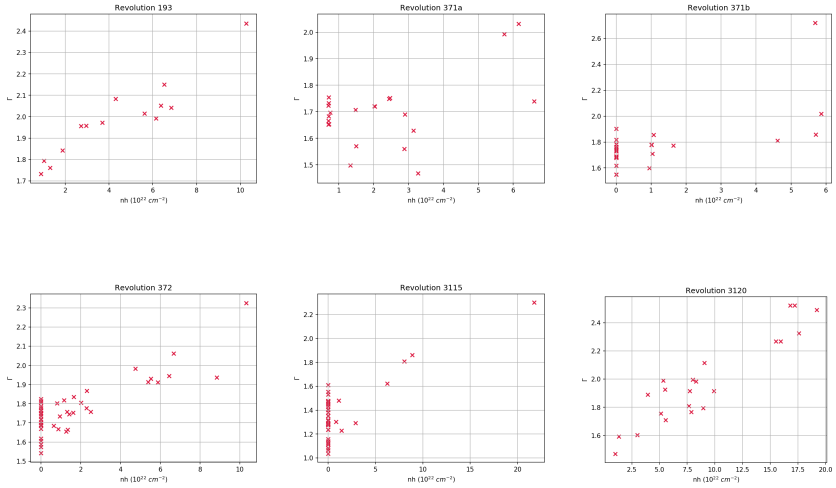

Figure 7.3: The photon index Γ plotted against the absorber column density N_H in each time bin, for all NGC 3783 observations. In the observations 371a, 371b, 372 and 3120 N_H is often consistent with 0- In the other cases, a strong correlation is present, due to the intrinsic degeneracy between these parameters.

energies between 6.3 keV and 6.4 keV for all spectra of each observation. We plotted this value vs. the photon index and no correlation appeared, as shown in Fig. 7.4 for NGC 3783 and Fig.7.5 for Mrk 509, respectively.

Then we made the same test considering the broadened line component. We compared the power law photon index with the intensity of the red tail of Fe Kα summing residuals from 5.6 keV to 6.0 keV. The resulting plots are shown in Fig. 7.6 for NGC 3783 and Fig.7.7 for Mrk 509, respectively; once again there are no indications of any kind of correlation.

For each observation we also calculated the Spearman correlation coefficient ρ_S between the values of Γ and the intensities of the two features. ρ_S varies between -1 and +1 with 0 implying no correlation between the datasets. Correlations of -1 or +1 imply an exact monotonic relationship. The values are reported in Tab.7.4 for NGC 3783 and Fig.7.5 for Mrk 509 respectively.

Considering all available datasets, the ρ_S are scattered around 0; their median values are listed in Tab. 7.6. Overall, we can say that we do not introduce any systematic error on this side.

Observation	**Number of spectra**	**Narrow line vs Γ** ρ_S	**Red wing vs Γ** ρ_S
193	14	-0.591	-0.560
371a	22	-0.301	0.322
371b	26	0.130	-0.081
372	50	-0.184	-0.152
3115	43	0.008	0.130
3120	22	-0.235	-0.426

Table 7.4: Values of ρ_S used to quantify the correlation between the photon index and the narrow line and red wing intensities for NGC 3783 observations.

Observation	**Number of spectra**	**Narrow line vs Γ** ρ_S	**Red wing vs Γ** ρ_S
161	11	0.164	0.545
250	17	-0.302	0.238
1073	34	0.259	0.134
1074	18	0.115	0.009
1168	27	0.117	0.066
1804	22	0.063	0.047
1806	25	0.382	0.318
1808	24	0.182	0.275
1811	24	-0.128	0.021
1813	24	0.138	-0.376
1815	25	0.492	-0.066
1817	24	-0.205	-0.081
1819	24	0.300	0.339
1821	26	-0.096	0.127
1822	24	0.355	0.150

Table 7.5: Values of ρ_S used to quantify the correlation between the photon index and the narrow line and red wing intensities for Mrk 509 observations.

Data	$< \rho_S >$
Narrow line vs Γ - NGC 3783	-0.195
Narrow line vs Γ - Mrk 509	0.122
Narrow line vs Γ - Total	-0.036
Red wing vs Γ - NGC 3783	-0.128
Red wing vs Γ - Mrk 509	0.116
Red wing vs Γ - Total	-0.006

Table 7.6: Mean values of ρ_S for the two sources (separately and treated together).

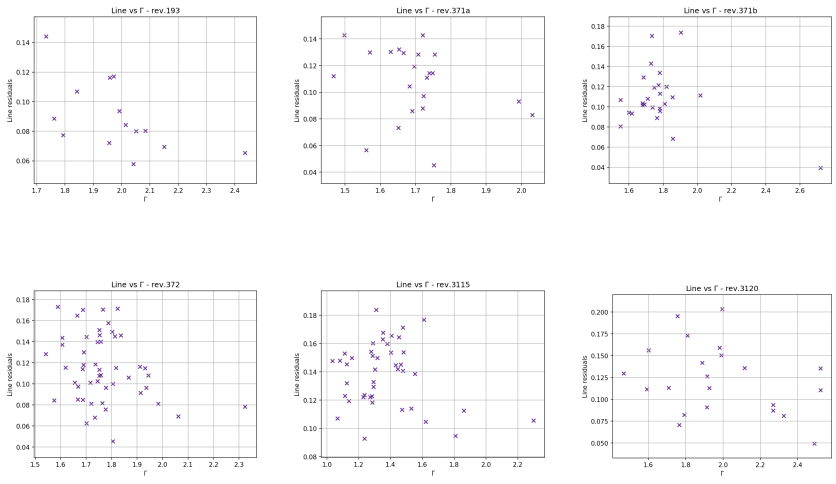

Figure 7.4: The photon index Γ plotted against the narrow Fe Kα line intensity, for each observation of NGC 3783. No correlation is evident.

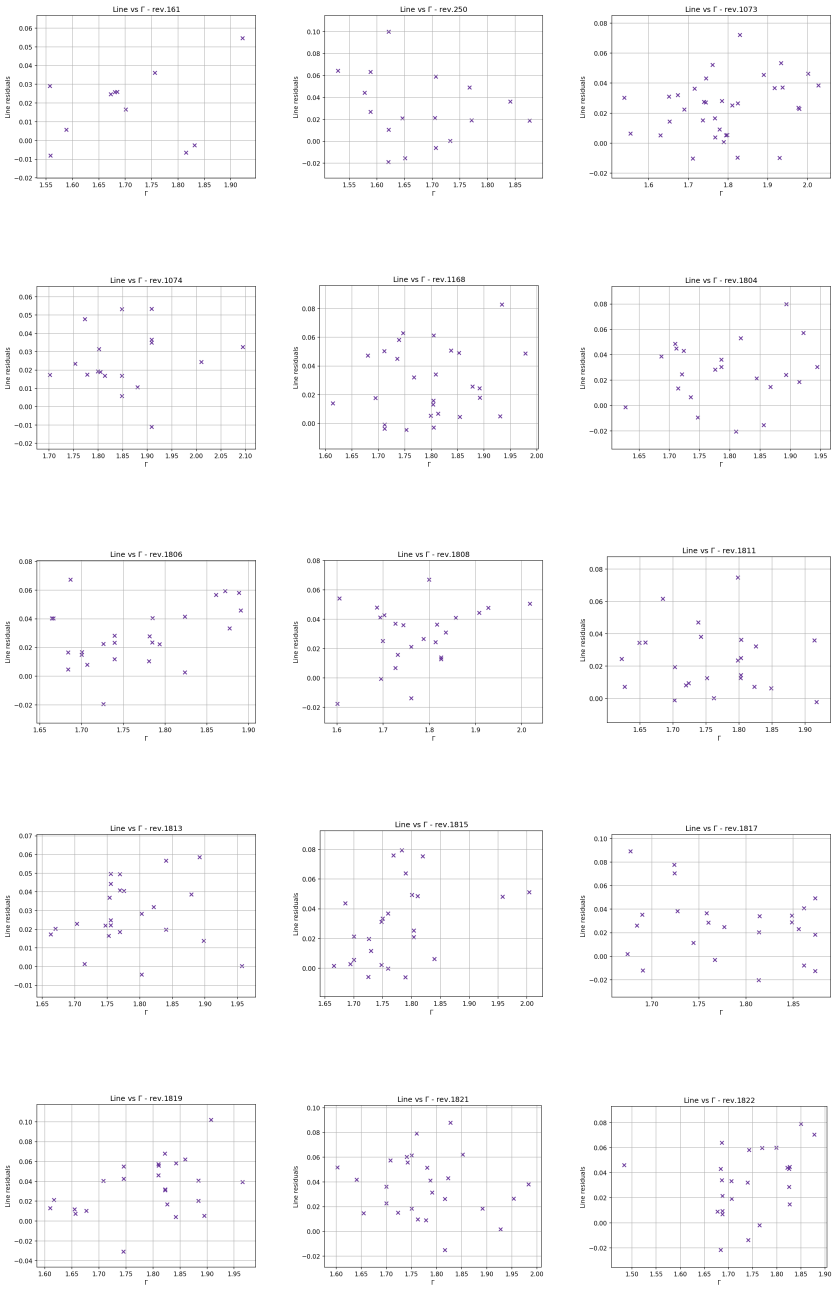

Figure 7.5: The photon index Γ plotted against the narrow Fe Kα line intensity, for each observation of Mrk 509. No correlation is evident.

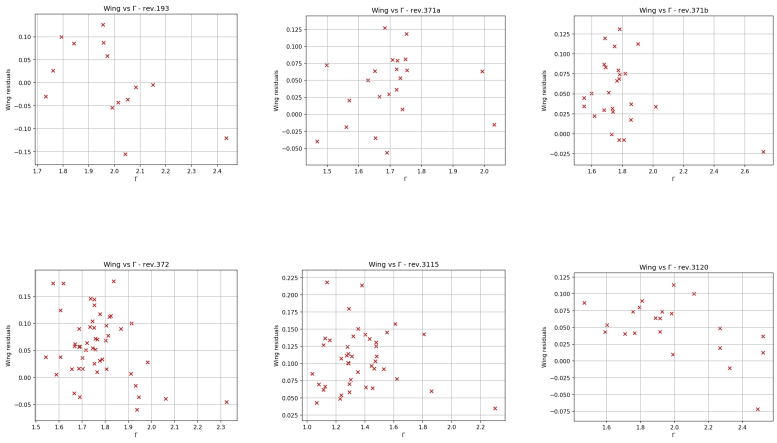

Figure 7.6: The photon index Γ plotted against the red wing feature intensity, for each observation of NGC 3783. No correlation is evident.

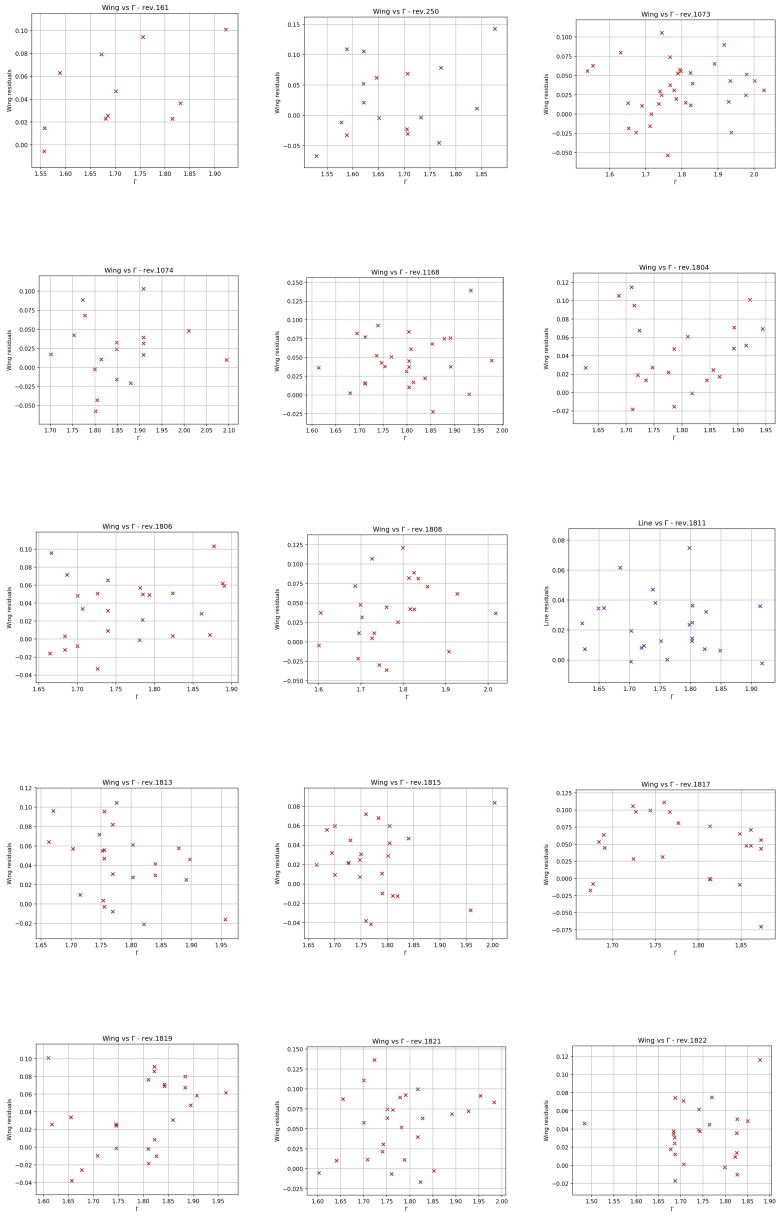

Figure 7.7: The photon index Γ plotted against the red wing feature intensity, for each observation of Mrk 509. No correlation is evident.

Chapter 8

Conclusions and future prospectives

In this thesis work we have faced the issue of probing the accretion/ejection flows in the inner regions of AGN, adopting a time-resolved spectral analysis technique.
The dynamics and the geometry of the material close to the SMBH are still largely uncertain, both for what concerns the inflows of the accretion disk and the outflows. For the latter phenomena it is important to understand their properties and their extent, as they are thought to have have a major role in the AGN feedback on galactic scales (e.g. King (2010)). A simultaneous investigation of these flows could bring some kind of correlation, that will help to better understand the driving mechanisms of massive winds from the disk, which is still an open issue of current high-energy astrophysics.
We carried our analysis in the 4.0-10.0 keV energy band, which includes the Fe Kα fluorescence emission line, a fundamental proxy of the motions around the SMBH, and possibly Fe resonant blueshifted absorption lines, features that are associated with the presence of UFOs.

We analyzed a selected sample of X-ray sources, using data acquired with XMM-*Newton*, i.e. the telescope with the highest sensitivity in our spectral range of interest, in order to probe variability on the shortest possible time scales. We selected the sources with a flux $\gtrsim 5 \times 10^{-12}$ erg s^{-1} in the 4.5-12.0 keV band and, among those, we chose those with the longest individual observations and the longest total exposure times, to follow variability on different time-scales. Using these criteria we selected NGC 3783 and Mrk 509. We added to our sample a third source with a significantly lower flux (one order of magnitude below our adopted threshold), but with the longest total exposure, over 2 Ms: IRAS 13224-3809, which has been extensively studied in recent years.

We found that for sources with a flux in our energy range as high as few 10^{-11} erg $s^{-1}cm^{-2}$ (i.e. NGC 3783 and Mrk 509) it is possible to use time bins as short as 2.5 ks and energy bins of 100 eV (the energy resolution in this band allowed by XMM-*Newton*) and still have a number of counts large enough to have significant statistics. On the other hand, for the source with the lowest X-ray flux ($\sim 10^{-13}$ erg $s^{-1}cm^{-2}$, i.e. IRAS 13224-3809), we are not able to achieve such fine resolution and we may carry out our variability analysis on longer time scales and losing information on most of the narrow features. The analysis carried out on IRAS 13224-3809 is meant to understand down to which fluxes we may use the technique adopted in this thesis work.
To probe the variability in the Fe K band, we use the *Excess maps technique* originally developed by Iwasawa et al. (2004), a time-resolved spectral analysis method. It is based on the representation of excess residuals against a spectral continuum modeled in a simple way in the time-energy domain. It allowed to spot sinusoidal variations of the excess in the 5.7-6.2 keV energy band with a period of ∼25 ks for the Seyfert 1 galaxy NGC 3516, interpreted as Doppler modulations of a Fe Kα line broadened by gravitational redshift and emitted at a distance from the SMBH in the range of 7-16 r_g. Excess maps were later used in other published works such as Turner et al. (2006), Tombesi et al. (2007) and De Marco et al. (2009).

We upgraded the original method and analyzed simultaneously the residuals above and below the continuum to simultaneously study both emission and absorption features. This approach is fundamental to have the broadest view of the innermost flows in AGN, since the information on the emission features has possibly a direct connection with that coming from the absorption features. We called our renewed procedure *Residual map technique*. We also improved the procedures of the continuum-fitting, by forcing the software to make a larger number of steps in the calculation of the best fit. The next natural step to improve the method, consists in providing a better fit for the continuum, probably implementing further components in the modeling to account for the spectral complexities observed in nearby AGN. We verified the reliability of our technique using several statistical tests, to check for possible systematics introduced in the analysis and for strong model-dependencies, as described in Chapter 7. Still aware that the technique is not perfect at present, we did not find relevant issues or evident dependance on the adopted model. We also made a direct comparison with classical spectral analysis, in section 4.2.1, that confirmed that the features we see in the residual maps are likely present also in the spectra and are not artifacts of the procedure.

Since one of the main goals of this work was to set up the new technique and test it, we decided to focus on one particular dataset of NGC 3783, in which we identified four Fe Kα line high peaks, spaced out by fairly regular

time intervals of $\sim$ 5-10 ks. Using equation 1.10 from Bardeen et al. (1972) for the computation of the orbital period at a fixed distance from the SMBH and considering a black hole mass of $\sim 3 \times 10^7 M_\odot$ (Peterson et al., 2004), we find that this emissivity could be originated in a range of $\sim$9-30 r_g.
We also performed a quick spectral inspection on one dataset of Mrk 509, whose map showed complex residual features in the whole map and a prominent Fe Kα component only in the second part of the observation. This change is present in the spectra as well, but it is not of easy explanation, calling for a further, detailed spectral analysis. The same analysis can be applied to the other datasets of NGC 3783 and Mrk 509 analyzed in this thesis work (without a proper comparison with X-ray spectral analysis),a lso a deeper analysis of absorption features can be carried out to search for possible high-velocity outflows.

A more complex spectral modeling is certainly needed to better characterize the sources and the physical phenomena in act, especially considering the high variability that these sources show on time scales even shorter than our 2.5 ks time bins. However, our residual maps can provide an immediate idea of the variability of the emission/absorption features and their time scales, and also provide hints on the components that may be used in the detailed spectral analysis.

XMM-*Newton* is continuing to acquire high quality data, so it will be possible to monitor the bright sources with this kind of analysis and possibly spot recursive features on longer time scales.
With the launch of *XRISM* (X-Ray Imaging and Spectroscopy Mission, previously named *XARM*), scheduled for 2021, thanks to the excellent spectral resolution of its detectors, it will be possible to resolve features as narrow as few eV on bright sources ($A_{eff} \sim 300$ cm^2 at 6 keV, about an half of the effective area of the EPIC pn on XMM-*Newton*).
In 2028, with the advent of *ATHENA* (Advanced Telescope for High Energy Astrophysics) and its unparalleled sensitivity ($A_{eff} \sim$0.25 m^2 at 6 keV), it will be possible to analyze sources with a low flux and/or probe shorter time scales for a much larger number of AGN.

Bibliography

Bardeen, J. M., Press, W. H. and Teukolsky, S. A. (1972), 'Rotating Black Holes: Locally Nonrotating Frames, Energy Extraction, and Scalar Synchrotron Radiation', *ApJ* **178**, 347–370.

Beckmann, V. and Shrader, C. (2013), *Active Galactic Nuclei*, Physics textbook, Wiley.
URL: *http://books.google.co.uk/books?id=QmwfxlZJM4sC*

Boissay, R., Paltani, S., Ponti, G., Bianchi, S., Cappi, M., Kaastra, J. S., Petrucci, P.-O., Arav, N., Branduardi-Raymont, G., Costantini, E., Ebrero, J., Kriss, G. A., Mehdipour, M., Pinto, C. and Steenbrugge, K. C. (2014), 'Multiwavelength campaign on Mrk 509. XIII. Testing ionized-reflection models on Mrk 509', *A & A* **567**, A44.

Boller, T. (1999), 'Spectral and timing properties of narrow-line Seyfert 1 galaxies.', *Memorie della Societá Astronomica Italiana* **70**, 1219–1222.

Boller, T., Brandt, W. N., Fabian, A. C. and Fink, H. H. (1997), 'ROSAT monitoring of persistent giant and rapid variability in the narrow-line Seyfert 1 galaxy IRAS 13224-3809', *MNRAS* **289**, 393–405.

Boller, T., Tanaka, Y., Fabian, A., Brandt, W. N., Gallo, L., Anabuki, N., Haba, Y. and Vaughan, S. (2003), 'XMM-Newton spectral properties of the narrow-line Seyfert 1 galaxy IRAS 13224 - 3809', *MNRAS* **343**, L89–L93.

Boller, T., Truemper, J., Molendi, S., Fink, H., Schaeidt, S., Caulet, A. and Dennefeld, M. (1993), 'Rapid X-ray variability in the I ZW 1 class object IRAS 13224-3809', *A & A* **279**, 53–60.

Brenneman, L. W., Reynolds, C. S., Nowak, M. A., Reis, R. C., Trippe, M., Fabian, A. C., Iwasawa, K., Lee, J. C., Miller, J. M., Mushotzky, R. F., Nandra, K. and Volonteri, M. (2011), 'The Spin of the Supermassive Black Hole in NGC 3783', *ApJ* **736**, 103.

Cappi, M. (2006), 'Relativistic blue- and red-shifted absorption lines in AGNs', *Astronomische Nachrichten* **327**, 1012.

Cappi, M., Tombesi, F., Bianchi, S., Dadina, M., Giustini, M., Malaguti, G., Maraschi, L., Palumbo, G. G. C., Petrucci, P. O., Ponti, G., Vignali, C. and Yaqoob, T. (2009), 'X-ray evidence for a mildly relativistic and variable outflow in the luminous Seyfert 1 galaxy Mrk 509', *A & A* **504**, 401–407.

Cooke, B. A., Ricketts, M. J., Maccacaro, T., Pye, J. P., Elvis, M., Watson, M. G., Griffiths, R. E., Pounds, K. A., McHardy, I., Maccagni, D., Seward, F. D., Page, C. G. and Turner, M. J. L. (1978), 'The Ariel V /SSI/ catalogue of high galactic latitude /absolute value of B greater than 10 deg/ X-ray sources', *MNRAS* **182**, 489–515.

Dadina, M., Cappi, M., Malaguti, G., Ponti, G. and de Rosa, A. (2005), 'X-ray absorption lines suggest matter infalling onto the central black-hole of Mrk 509', *A & A* **442**, 461–468.

De Marco, B., Iwasawa, K., Cappi, M., Dadina, M., Tombesi, F., Ponti, G., Celotti, A. and Miniutti, G. (2009), 'Probing variability patterns of the Fe K line complex in bright nearby AGNs', *A & A* **507**, 159–169.

Dewangan, G. C., Boller, T., Singh, K. P. and Leighly, K. M. (2002), 'A 10-day ASCA observation of the narrow-line Seyfert 1 galaxy IRAS 13224-3809', *A & A* **390**, 65–80.

Fabian, A. C., Iwasawa, K., Reynolds, C. S. and Young, A. J. (2000), 'Broad Iron Lines in Active Galactic Nuclei', *Publication of the Astronomical Society of the Pacific* **112**, 1145–1161.

Gallo, L. C. (2004), 'The X-ray timing properties of the NLS1s IRAS 13224-3809 and I Zw 1', *Memorie della Societá Astronomica Italiana* **75**, 523.

Gallo, L. C. (2006), 'Investigating the nature of narrow-line Seyfert 1 galaxies with high-energy spectral complexity', *MNRAS* **368**, 479–486.

George, I. M., Turner, T. J., Netzer, H., Nandra, K., Mushotzky, R. F. and Yaqoob, T. (1998), 'ASCA Observations of Seyfert 1 Galaxies. III. The Evidence for Absorption and Emission Due to Photoionized Gas', *ApJS* **114**, 73–120.

Haardt, F. and Maraschi, L. (1991), 'A two-phase model for the X-ray emission from Seyfert galaxies', *ApJL* **380**, L51–L54.

Haardt, F. and Maraschi, L. (1993), 'X-ray spectra from two-phase accretion disks', *ApJ* **413**, 507–517.

Iwasawa, K., Miniutti, G. and Fabian, A. C. (2004), 'Flux and energy modulation of redshifted iron emission in NGC 3516: implications for the black hole mass', *MNRAS* **355**, 1073–1079.

Kaastra, J. S., Petrucci, P.-O., Cappi, M., Arav, N., Behar, E., Bianchi, S., Bloom, J., Blustin, A. J., Branduardi-Raymont, G., Costantini, E., Dadina, M., Detmers, R. G., Ebrero, J., Jonker, P. G., Klein, C., Kriss, G. A., Lubiński, P., Malzac, J., Mehdipour, M., Paltani, S., Pinto, C., Ponti, G., Ratti, E. M., Smith, R. A. N., Steenbrugge, K. C. and de Vries, C. P. (2011), 'Multiwavelength campaign on Mrk 509. I. Variability and spectral energy distribution', *A & A* **534**, A36.

Kaspi, S., Brandt, W. N., Netzer, H., George, I. M., Chartas, G., Behar, E., Sambruna, R. M., Garmire, G. P. and Nousek, J. A. (2001), 'High-Resolution X-Ray Spectroscopy and Modeling of the Absorbing and Emitting Outflow in NGC 3783', *ApJ* **554**, 216–232.

Kaspi, S., Smith, P. S., Netzer, H., Maoz, D., Jannuzi, B. T. and Giveon, U. (2000), 'Reverberation Measurements for 17 Quasars and the Size-Mass-Luminosity Relations in Active Galactic Nuclei', *ApJ* **533**, 631–649.

King, A. R. (2010), 'Black hole outflows', *MNRAS* **402**, 1516–1522.

Makishima, K. (1986), Iron Lines from Galactic and Extragalactic X-ray Sources, *in* K. O. Mason, M. G. Watson and N. E. White, eds, 'The Physics of Accretion onto Compact Objects', Vol. 266 of *Lecture Notes in Physics, Berlin Springer Verlag*, p. 249.

Mathur, S. (2000), 'Narrow-line Seyfert 1 galaxies and the evolution of galaxies and active galaxies', *MNRAS* **314**, L17–L20.

McHardy, I. M., Lawrence, A., Pye, J. P. and Pounds, K. A. (1981), 'The Ariel V /3 A/ catalogue of X-ray sources. II - Sources at high galactic latitude /absolute value of B greater than 10 deg/', *MNRAS* **197**, 893–919.

Mehdipour, M., Kaastra, J. S., Kriss, G. A., Arav, N., Behar, E., Bianchi, S., Branduardi-Raymont, G., Cappi, M., Costantini, E., Ebrero, J., Di Gesu, L., Kaspi, S., Mao, J., De Marco, B., Matt, G., Paltani, S., Peretz, U., Peterson, B. M., Petrucci, P.-O., Pinto, C., Ponti, G., Ursini, F., de Vries, C. P. and Walton, D. J. (2017), 'Chasing obscuration in type-I AGN: discovery of an eclipsing clumpy wind at the outer broad-line region of NGC 3783', *A & A* **607**, A28.

Morini, M., Lipani, N. A. and Molteni, D. (1987), 'The X-ray spectrum of Markarian 509 observed by EXOSAT', *ApJ* **317**, 145–151.

Mushotzky, R. F., Done, C. and Pounds, K. A. (1993), 'X-ray spectra and time variability of active galactic nuclei', *ARAA* **31**, 717–761.

Padovani, P., Alexander, D. M., Assef, R. J., De Marco, B., Giommi, P., Hickox, R. C., Richards, G. T., Smolčić, V., Hatziminaoglou, E., Mainieri, V. and Salvato, M. (2017), 'Active galactic nuclei: what's in a name?', *The Astronomy and Astrophysics Review* **25**, 2.

Page, M. J., Davis, S. W. and Salvi, N. J. (2003), 'The origin of the Fe K features in Markarian 205 and Markarian 509', *MNRAS* **343**, 1241–1247.

Parker, M. L., Alston, W. N., Buisson, D. J. K., Fabian, A. C., Jiang, J., Kara, E., Lohfink, A., Pinto, C. and Reynolds, C. S. (2017), 'Revealing the ultrafast outflow in IRAS 13224-3809 through spectral variability', *MNRAS* **469**, 1553–1558.

Peterson, B. (1997), *An Introduction to Active Galactic Nuclei*, Cambridge University Press.

Peterson, B. M., Ferrarese, L., Gilbert, K. M., Kaspi, S., Malkan, M. A., Maoz, D., Merritt, D., Netzer, H., Onken, C. A., Pogge, R. W., Vestergaard, M. and Wandel, A. (2004), 'Central Masses and Broad-Line Region Sizes of Active Galactic Nuclei. II. A Homogeneous Analysis of a Large Reverberation-Mapping Database', *ApJ* **613**, 682–699.

Petrucci, P.-O., Paltani, S., Malzac, J., Kaastra, J. S., Cappi, M., Ponti, G., De Marco, B., Kriss, G. A., Steenbrugge, K. C., Bianchi, S., Branduardi-Raymont, G., Mehdipour, M., Costantini, E., Dadina, M. and Lubiński, P. (2013), 'Multiwavelength campaign on Mrk 509. XII. Broad band spectral analysis', *A & A* **549**, A73.

Piccinotti, G., Mushotzky, R. F., Boldt, E. A., Holt, S. S., Marshall, F. E., Serlemitsos, P. J. and Shafer, R. A. (1982), 'A complete X-ray sample of the high-latitude /absolute value of B greater than 20 deg/ sky from HEAO 1 A-2 - Log N-log S and luminosity functions', *ApJ* **253**, 485–503.

Pinto, C., Alston, W., Parker, M. L., Fabian, A. C., Gallo, L. C., Buisson, D. J. K., Walton, D. J., Kara, E., Jiang, J., Lohfink, A. and Reynolds, C. S. (2018), 'Ultrafast outflows disappear in high-radiation fields', *MNRAS* **476**, 1021–1035.

Ponti, G., Cappi, M., Costantini, E., Bianchi, S., Kaastra, J. S., De Marco, B., Fender, R. P., Petrucci, P.-O., Kriss, G. A., Steenbrugge, K. C., Arav, N., Behar, E., Branduardi-Raymont, G., Dadina, M., Ebrero, J., Lubiński, P., Mehdipour, M., Paltani, S., Pinto, C. and Tombesi, F. (2013), 'Multiwavelength campaign on Mrk 509. XI. Reverberation of the Fe Kα line', *A & A* **549**, A72.

Ponti, G., Gallo, L. C., Fabian, A. C., Miniutti, G., Zoghbi, A., Uttley, P., Ross, R. R., Vasudevan, R. V., Tanaka, Y. and Brandt, W. N. (2010),

'Relativistic disc reflection in the extreme NLS1 IRAS13224-3809', *MNRAS* **406**, 2591–2604.

Pounds, K. A., Nandra, K., Fink, H. H. and Makino, F. (1994), 'Constraining the complexities in Seyfert X-ray spectra - an analysis of simultaneous observations with GINGA and ROSAT', *MNRAS* **267**, 193.

Pounds, K., Reeves, J., O'Brien, P., Page, K., Turner, M. and Nayakshin, S. (2001), 'An XMM-Newton Observation of the Luminous Seyfert 1 Galaxy Markarian 509', *ApJ* **559**, 181–186.

Reeves, J. N., Nandra, K., George, I. M., Pounds, K. A., Turner, T. J. and Yaqoob, T. (2004), 'The XMM-Newton Iron Line Profile of NGC 3783', *ApJ* **602**, 648–658.

Reynolds, C. S. (1997), Warm Absorbers in Seyfert 1 Galaxies, *in* N. Arav, I. Shlosman and R. J. Weymann, eds, 'Mass Ejection from Active Galactic Nuclei', Vol. 128 of *Astronomical Society of the Pacific Conference Series*, p. 173.

Rosen, S. R., Webb, N. A., Watson, M. G., Ballet, J., Barret, D., Braito, V., Carrera, F. J., Ceballos, M. T., Coriat, M., Della Ceca, R., Denkinson, G., Esquej, P., Farrell, S. A., Freyberg, M., Grisé, F., Guillout, P., Heil, L., Koliopanos, F., Law-Green, D., Lamer, G., Lin, D., Martino, R., Michel, L., Motch, C., Nebot Gomez-Moran, A., Page, C. G., Page, K., Page, M., Pakull, M. W., Pye, J., Read, A., Rodriguez, P., Sakano, M., Saxton, R., Schwope, A., Scott, A. E., Sturm, R., Traulsen, I., Yershov, V. and Zolotukhin, I. (2016), 'The XMM-Newton serendipitous survey. VII. The third XMM-Newton serendipitous source catalogue', *A & A* **590**, A1.

Singh, K. P., Garmire, G. P. and Nousek, J. (1985), 'Observation of soft X-ray spectra from a Seyfert 1 and a narrow emission-line galaxy', *ApJ* **297**, 633–638.

Tombesi, F., Cappi, M., Reeves, J. N., Palumbo, G. G. C., Yaqoob, T., Braito, V. and Dadina, M. (2010), 'Evidence for ultra-fast outflows in radio-quiet AGNs. I. Detection and statistical incidence of Fe K-shell absorption lines', *A & A* **521**, A57.

Tombesi, F., de Marco, B., Iwasawa, K., Cappi, M., Dadina, M., Ponti, G., Miniutti, G. and Palumbo, G. G. C. (2007), 'Correlated modulation between the redshifted Fe Kα line and the continuum emission in NGC 3783', *A & A* **467**, 1057–1063.

Turner, T. J., Miller, L., George, I. M. and Reeves, J. N. (2006), 'Evidence for orbital motion of material close to the central black hole of Mrk 766', *A & A* **445**, 59–67.

Turner, T. J., Nandra, K., George, I. M., Fabian, A. C. and Pounds, K. A. (1993), 'X-Ray Observations of the Warm Absorber in NGC 3783', *ApJ* **419**, 127.

Woo, J.-H. and Urry, C. M. (2002), 'Active Galactic Nucleus Black Hole Masses and Bolometric Luminosities', *ApJ* **579**, 530–544.

Zhou, X.-L. and Wang, J.-M. (2005), 'Narrow Iron Kα Lines in Active Galactic Nuclei: Evolving Populations?', *ApJL* **618**, L83–L86.